Vortex Dominated Aeolian Activity at InSight's Landing Site, Part 2: Local Meteorology, Transport Dynamics, and Model Analysis

M. Baker, C. Newman, C. Charalambous, M. Golombek, A. Spiga, D. Banfield, M. Lemmon, M. Banks, R. Lorenz, J. Garvin, et al.

JGR Planets

RESEARCH ARTICLE
10.1029/2020JE006514

Special Section:
InSight at Mars

Vortex-Dominated Aeolian Activity at InSight's Landing Site, Part 2: Local Meteorology, Transport Dynamics, and Model Analysis

M. Baker[1,2], C. Newman[3], C. Charalambous[4], M. Golombek[5], A. Spiga[6], D. Banfield[7], M. Lemmon[8], M. Banks[9], R. Lorenz[10], J. Garvin[9], J. Grant[1], K. Lewis[2], V. Ansan[11], N. Warner[12], C. Weitz[13], S. Wilson[1], and S. Rodriguez[14]

[1]Center for Earth & Planetary Studies, National Air & Space Museum, Smithsonian Institution, Washington, DC, USA, [2]The Morton K. Blaustein Department of Earth & Planetary Sciences, Johns Hopkins University, Baltimore, MD, USA, [3]Aeolis Research, Pasadena, CA, USA, [4]Imperial College, London, UK, [5]Jet Propulsion Laboratory, California Institute of Technology, Pasadena, CA, USA, [6]Laboratoire de Meteorologie Dynamique, Paris, France, [7]Cornell Center for Astrophysics & Planetary Science, Cornell University, Ithaca, NY, USA, [8]Space Science Institute, Boulder, CO, USA, [9]NASA Goddard Space Flight Center, Greenbelt, MD, USA, [10]Johns Hopkins University Applied Physics Laboratory, Laurel, MD, USA, [11]Laboratoire de Planétologie et de Géodynamique de Nantes, Nantes, France, [12]Department of Geological Sciences, SUNY Geneseo, Geneseo, NY, USA, [13]Planetary Science Institute, Tucson, AZ, USA, [14]Université de Paris, Institut de Physique du Globe de Paris, CNRS, Paris, France

Abstract Geologic and climatic processes on modern-day Mars are heavily influenced by aeolian surface activity, yet the relationship between atmospheric conditions and sediment mobilization is not well understood. The Interior Exploration using Seismic Investigations, Geodesy, and Heat Transport (InSight) spacecraft is uniquely able to address this issue, due to its joint imaging and continuous high-frequency meteorological capabilities, which allow for direct comparison between surface activity and atmospheric conditions. Since landing in the volcanic plains of Elysium Planitia, InSight's camera's have recorded intermittent, small-scale surface changes, including removal of fine material on the lander footpad, linear tracks and localized surface darkening caused by minor dust removal, and surface creep of granules, as presented in Part 1 (Charalambous et al., 2021, this issue). Surface activity is found to correlate well with the timing of abrupt pressure drops ($\Delta P \sim 1$–9 Pa) and transient wind gusts ($v \sim 14$–31 m/s) associated with convective vortex passage. Here we identify the major erosive forces acting on surface particles during these events, including the vertical pressure gradient force at the vortex core and the drag force generated by quickly-rotating tangential winds. Orbital and ground-truth data suggest that aeolian activity at InSight's landing site is sporadic under modern climatic conditions. Ongoing aeolian surface modifcation is driven primarily by turbulent vortices that sporadically lift dust and redistribute coarser sediment (i.e., sand and granules) but do not aid in the development of organized aeolian bedforms. Surface erosion is localized within the path these vortices take across the surface which is controlled by seasonally-reversing background circulation patterns.

Plain Language Summary Numerous orbiting and landed spacecraft have imaged wind-driven ("aeolian") motion of sand and dust on Mars. However, spacecraft on the surface have generally lacked the instrumentation required to interpret the atmospheric conditions driving this motion. Here we utilize the unique opportunity provided by the NASA InSight lander's joint imaging and meteorological capabilities to closely interpret ongoing aeolian activity at the spacecraft's landing site at Elysium Planitia and similar plains regions across Mars. During the first 400 martian days (sols) of the mission, intermittent, small-scale motion of dust and sand are observed in association with local, thermally driven vortices passing over or near the lander. In situ data are also compared to orbital images and atmospheric model predictions to obtain a more comprehensive picture of wind-related processes across the region. Overall, aeolian surface modification at this location is found to be very limited under current climatic conditions and is likely dominated by redistribution of fine material caused by transient convective events.

Key Points:

- NASA's InSight mission provides a chance to study aeolian transport through concurrent imaging and high-frequency atmospheric monitoring
- The surface at InSight's landing site is generally stable besides intermittent surface activity caused by convective vortex passage
- The vertical pressure gradient within the vortex core and increased drag caused by rotational winds help facilitate surface erosion

Supporting Information:

- Supporting Information S1
- Movie S1
- Movie S2
- Movie S3
- Movie S4

Correspondence to:
M. Baker,
bakerm@si.edu

Citation:
Baker, M., Newman, C., Charalambous, C., Golombek, M., Spiga, A., Banfield, D., et al. (2021). Vortex-dominated aeolian activity at InSight's landing site, Part 2: Local meteorology, transport dynamics, and model analysis. *Journal of Geophysical Research: Planets*, *126*, e2020JE006514. https://doi.org/10.1029/2020JE006514

Received 8 MAY 2020
Accepted 2 DEC 2020

1. Introduction

Prior to robotic exploration, transient color variations observed from Earth-based telescopes provided potential evidence of active wind-driven surface processes on Mars (Antoniadi, 1930; McLaughlin, 1954; Pollack & Sagan, 1967). Spacecraft sent to Mars in the 1960s and 1970s provided our first real look at the planet's dry and cratered modern surface. Wind streaks, circumpolar dune fields, and significantly infilled craters implied a long aeolian history (Breed et al., 1979; Cutts & Smith, 1973; Leighton et al., 1965; Tsoar et al., 1979). Over geologic timescales, a significant volume of wind-blown material had been removed from plains regions, and redeposited into sediment sinks within topographic lows and sand seas ("ergs"). Subsequent orbiters equipped with progressively higher-resolution imaging capabilities brought the martian surface into focus, revealing a diversity of aeolian landscapes across the planet, including some with relatively fresh morphologies (Edgett & Blumberg, 1994). Despite early observations of columnar dust devils and global dust storms (Leovy et al., 1973; Thomas & Gierasch, 1985), repeat "change detection" images were unable to detect movement in martian dunes, leading many to hypothesize that tenuous contemporary winds were generally incapable of mobilizing aeolian bedforms (Ward & Doyle, 1983; Zimbelman, 2000), even if sporadic dust entrainment could be triggered by exceptional environmental conditions. However, after more than a decade in operation, interpretation of High-Resolution Imaging Science Experiment (HiRISE) images finally allowed confident detection of dune and ripple migration across the planet (e.g., Bridges et al., 2012; Silvestro et al., 2016, and many others). Still, the coarse spatial and temporal resolution of orbital images has made it difficult to constrain the nature and frequency of individual transport events. This is especially true given the dynamic nature of the martian climate system, which is characterized by annual, seasonal, and diurnal variability in circulation patterns, as well as atmospheric phenomena that are more episodic or stochastic in nature (e.g., global dust storms).

Ground-truth data acquired by landed spacecraft have provided invaluable insight into the nature of ongoing aeolian modification across geomorphically distinct regions of Mars. Meteorological data acquired by the dual Viking spacecraft enabled measurement of wind speed and direction over a short time period after landing as well as detection of over one hundred convective vortices on the surface (Ryan & Lucich, 1983; Zurek et al., 1992). It has long been understood that passing convective vortices can cause abrupt drops in atmospheric pressure and changes in wind speed/direction (Gierasch & Goody, 1973), but the peak wind speeds measured by the Viking spacecraft during vortex passage typically did not reach the traditional threshold for dust lifting, suggesting that a majority of these vortices were likely not dust-loaded (Ryan & Lucich, 1983). Background wind speeds at both sites were generally low, consistent with the observed stability of the surface, although in one instance, a strong wind gust was able to mobilize sand that had been placed on the Viking 1 lander deck (Sagan et al., 1977). After 5 years on the surface, Viking 1 cameras recorded erosion of disturbed sediment piles and widespread redistribution of surface dust during a global dust storm event (Arvidson et al., 1983; Moore et al., 1985), suggesting that ongoing aeolian modification at this site was dominated by such episodic meteorological phenomena. Unfortunately, by the time this storm occurred the lander's wind sensor had ceased operations, thus no wind speed data were available to interpret observed changes.

Wind speeds measured by the subsequent Mars Pathfinder (MPF) and Phoenix landers were also typically very low (Greeley et al., 2000; Holstein-Rathlou et al., 2010), which was again consistent with the lack surface changes observed in lander images (Sullivan et al., 2000). However, at the MPF landing site, vortices were detected in pressure data (Murphy & Nelli, 2002; Schofield & Barnes, 1997) and active dust devils were observed in images for the first time on the martian surface (Metzger et al., 1999). Unfortunately, the spacecraft had no overlapping meteorological data with which to understand the mechanisms responsible for observed dust lifting. Vortices were also detected in meteorological data acquired by the Phoenix spacecraft, but measured winds during these events never exceeded traditional thresholds for dust entrainment (Ellehoj et al., 2010). Cameras onboard the Mars Exploration Rovers Spirit and Opportunity did capture some evidence of aeolian activity, including short-trajectory motion of surface grains, redistribution of surface dust, active dust devils, and small-scale ripple migration (Geissler et al., 2010; Greeley et al., 2010, 2006; Sullivan et al., 2008). Unfortunately, neither MER rover was equipped with a meteorological sensor, making it impossible to directly meaure the atmospheric conditions (i.e., wind speed and atmospheric pressure) present during sediment mobilization.

Unlike the spacecraft that came before, the Mars Science Laboratory (MSL) Curiosity rover has observed widespread sand transport at its landing site within Gale crater (Baker et al., 2018a). In particular, MSL provided the first in situ observations within an active martian dune field (Bridges et al., 2017), where ripples were observed to migrate daily during southern summer (Baker et al., 2018b). While it has been well-established that aeolian surface modification in Gale crater is a recurring seasonal phenomenon and that aeolian threshold conditions are being regularly exceeded at this location, it has still not been possible to constrain the winds driving this motion due to significant gaps and calibration issues in the rover's wind data (Newman et al., 2017). Whereas the Remote Environmental Monitoring System (REMS) instrument onboard MSL has recorded pressure drops indicative of passing vortices, the vast majority of vortices were inferred to be dust free (Streakley & Murphy 2016), consistent with the lack of dust devils or dust devil tracks identified within orbital or ground images (Moores et al., 2015). Possible explanations for this include weaker vortex strength compared to other landing sites (Kahanpää et al., 2016), varied dust availability (Streakley & Murphy 2016), or observational biases caused by camera pointing (Newman et al., 2019).

Overall, images returned from landed and orbiting cameras have revealed a diversity of wind-induced features across the Martian surface, including dust devil tracks, wind streaks, Transverse Aeolian Ridges (TARs), and dunes. Mobilization of sediment is uniquely tied to both local climatic conditions and surface properties, such that the nature and frequency of aeolian activity varies significantly from site to site. In some locations on Mars (e.g., Gale crater), wind is actively driving landscape modification through significant sand transport and dust lifting, despite the fact that atmospheric model predictions and limited in situ wind measurements are not able to explain high levels of activity (Baker et al., 2018b; Fenton et al., 2005; Haberle et al., 1993; Newman et al., 2002). In particular, data suggest that contemporary winds rarely exceed the traditional motion thresholds for even the most easily-mobilized material (i.e., particles 100–150 μm in diameter typical of modern aeolian bedforms on both Earth and Mars), much less for dust (i.e., particles < 4 μm in diameter), which has a significantly higher threshold due to increased interparticle forces (Bagnold 1941; Shao & Lu, 2000).

Many ideas have been put forward to reconcile the discrepancy between low winds and observed dust lifting, including mobilization of dust through sand-blasting, aggregation of dust particles, and the vortex "suction effect" or "delta-P effect" caused by the pressure difference below and above surface grains (Balme & Hagermann 2006; Greeley et al., 2003, 2002; Hsu et al., 1976; Neakrase & Greeley 2010). With respect to sand transport, results from recent numerical modeling and laboratory experiments have suggested that the lower gravity on Mars could facilitate the initiation and continuation of sand motion at lower wind speeds than previously predicted (Almeida et al., 2008; Kok et al., 2010; Musiolik et al., 2018; Sullivan & Kok, 2017; Swann et al., 2020). Although these studies have advanced our understanding of martian aeolian physics, validating these various hypotheses requires detailed examination of these processes in action on Mars. The Interior Exploration using Seismic Investigations, Geodesy, and Heat Transport (InSight) spacecraft is uniquely posed to investigate aeolian activity due to its joint imaging and high-frequency, continuous meteorological capabilities. Synchronous in situ atmospheric and surface monitoring enables robust correlation between environmental conditions and resultant modification, which is essential for achieving a mechanistic understanding of wind-driven transport and for interpreting aeolian landscapes seen across Mars.

The flat, volcanic terrain of Elysium Planitia, where InSight landed in 2018 (Banerdt et al., 2020; Golombek et al., 2017, 2020), is morphologically similar to many other plains regions across Mars (Tanaka et al., 2014). The surface exhibits little topographic relief and is primarily composed of poorly consolidated material (i.e., sand) with a thin cover of optically thick dust (Christensen et al., 2004; M. Golombek et al., 2017, 2018, 2020). The InSight landing site (informally named *Homestead hollow*) is located in the northern lowlands (4.502°N, 135.623°E) at an elevation of −2,163.43 m with respect to the Mars Orbiter Laser Altimeter (MOLA) geoid. The region around *Homestead hollow* is characterized craters of varying ages and degradation states, some of which have rocky ejecta (Figures 1b and 1e); *Homestead hollow* itself is an example of the most degraded class of impact crater (Warner et al., 2020,this issue) and, like many other nearby hollows, has experienced significant aeolian infilling that has equilibrated the surface with the prevailing wind regime (Grant et al., 2020, this issue). Upon landing, images revealed a "smooth" terrain within the hollow interior, characterized by fine sand and pebbles overlying more cohesive material, and a "rocky" terrain exterior to the degraded crater rim (Golombek et al., 2020; Grant et al., 2020, this issue; Warner et al., 2020

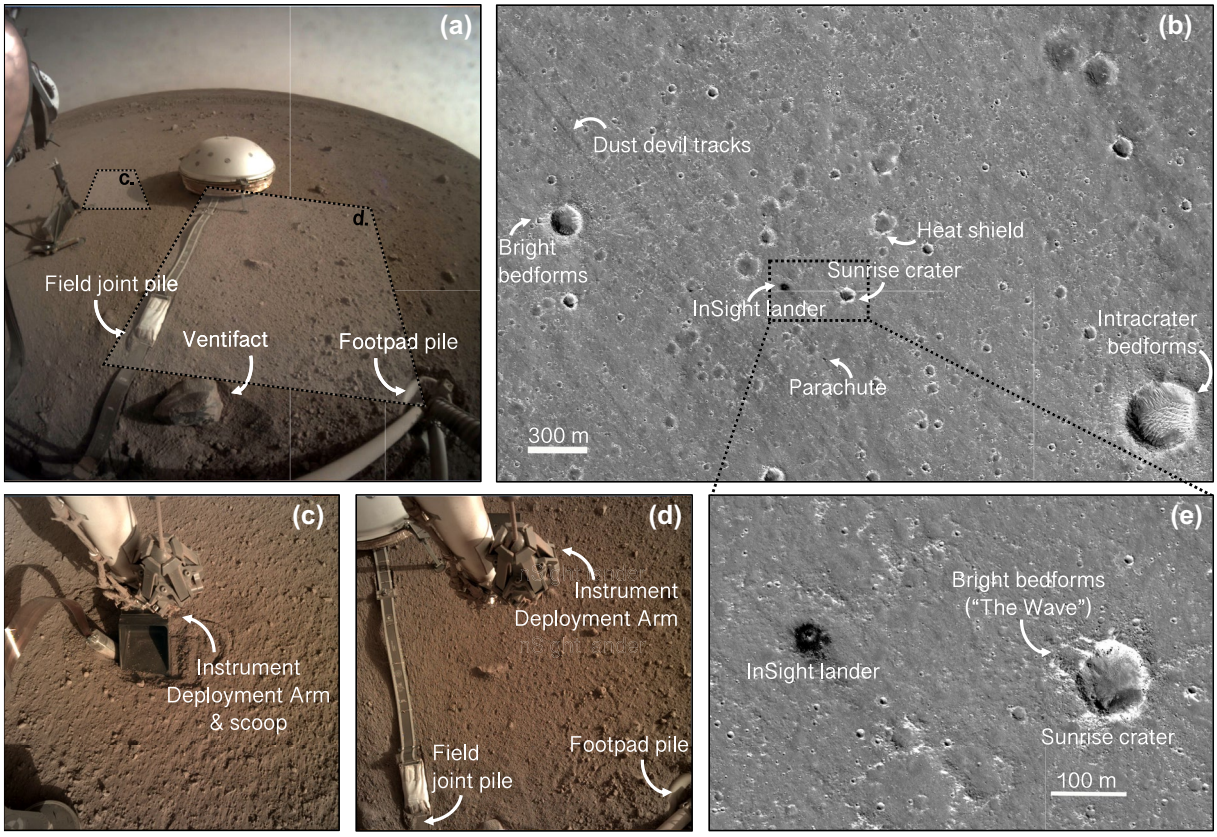

Figure 1. Examples of surface and orbital change detection images. (a) Standard ICC workspace image (C000M0118_607018617EDR_F0000_0704M) acquired on Sol 118 (b) HiRISE image ESP_062528_1845. (c) Opportunistic IDC image (D000M0387_630895798EDR_F0000_0250M) acquired during mole pinning on Sol 387. (d) IDC retirement pose (D000M0166_611280224EDR_F0000_0250M) acquired on Sol 166. (e) Subset of HiRISE image ESP_062528_1845 zoomed in on Homestead hollow and nearby bright bedforms ("The Wave") on the northwest side of Sunrise crater. Although the lack of modern aeolian bedforms within the lander workspace and across the region suggests the surface is relatively stable, ventifacts and smooth crater fill imply higher levels of aeolian activity in the past. HiRISE, High-Resolution Imaging Science Experiment; ICC, Instrument Context Camera; IDA, Instrument Deployment Arm.

this issue). There were no obvious aeolian bedforms in the workspace, but two potential ventifacts could be seen beneath the lander ("Ace of Spades Rock" and "Turtle Rock"), consistent with previous aeolian activity indicated by crater degradation and infilling.

Despite the region's inferred aeolian history, the modern surface exhibits relatively few aeolian features at regional scale (Golombek et al., 2018, 2020; Banks et al., 2019; Grant et al., 2020, this issue; Warner et al., 2020 this issue); some potential bedforms can be observed within the ejecta blankets and on the floors of nearby craters, but a majority of these are light-toned, suggesting high levels of dust cover and stability. High-albedo bedforms adjacent to craters predominantly exist on the west and northwest side of crater rims; one such feature ("The Wave") is located ~400 m to the southeast of *Homestead hollow* on the northwest side of Sunrise crater and can be resolved in lander images (Golombek et al., 2020). Similar bright bedforms, but with smaller wavelengths, also appear on the floors of moderately degraded craters (Banks et al., 2019). Lower-albedo ripples with relatively fresh morphologies are observed in HiRISE images in some of the most pristine to moderately degraded craters, typically trending northeast-southwest (Sweeney et al., 2018; Banks et al., 2019; Grant et al., 2020, this issue; Warner et al., 2020 this issue). Bedform orientations are generally consistent with prelanding atmospheric predictions of dominant regional winds that alternate seasonally between northwesterlies and southeasterlies (Golombek et al., 2018; Spiga et al., 2018; Perrin et al., 2020, this issue). This seasonality has been further confirmed by meteorological data acquired thus far by InSight instruments (Banfield et al., 2020), and is also consistent with the dominant direction and formation rate of dust devil tracks observed from orbit (Reiss & Lorenz, 2016; Perrin et al., 2020, this issue). Orbital analyses

suggest that this region is dominated by small (<10 m) dust devils and that dust clearing events may be relatively rarer compared to some other landing sites.

Coordinated change detection experiments have been conducted from the InSight lander since its arrival on Mars. A detailed description of observed surface changes, as well as the atmospheric conditions responsible for these changes, is presented in the companion paper (Part 1; Charalambous et al., 2021, this issue). Here we combine ground-truth data from the first 400 sols of the mission, atmospheric model predictions, and orbital data acquired over three Mars years to understand how observations of sediment motion fit within the larger context of the meteorology at the landing site and the geomorphology of the region. Although intermittent sediment mobilization is observed in association with passing convective vortices, the surface at *Homestead hollow* is found to be relatively stable under current climatic conditions. Through close examination of the atmospheric conditions present during observed motion and comparison between these conditions and current transport models, we are able to shed light on the nature of aeolian activity at *Homestead hollow* and probe the dynamics of sediment transport on modern-day Mars more generally.

2. Methodology

2.1. InSight Change Detection Imaging

The InSight lander's Instrument Deployment System (IDS) contains two cameras that can be used to search for wind-induced changes in surface sediment around the lander (Maki et al., 2018). The Instrument Context Camera (ICC) is hard-mounted below the lander deck and has a 120° field of view (FOV) covering the entire deployment workspace (Figure 1a). ICC workspace images have been acquired regularly since the start of the mission, providing a large data set of images that can be used for change detection. The Instrument Deployment Camera (IDC) is positioned on the forearm of the Instrument Deployment Arm (IDA) and has an FOV of 45° (Figure 1b). ICC and IDC images acquired under consistent illumination conditions are compared directly to search for obvious movement in surface sediment in the lander's vicinity (Charalambous et al., 2021, this issue). Although standard ICC workspace images are not able to the resolve individual sand grains, some IDC images that have been used to monitor engineering activities have provided opportunistic, higher-resolution change detection images within the workspace. As the lander's workspace was found to be devoid of aeolian bedforms, change detection experiments have paid particular attention to monitoring disturbed areas, including around where the Heat Flow and Physical Properties Package was deployed and where artificial sediment piles accumulated on the west footpad after landing and on the seismometer tether after it was partially retracted on Sol 59. An IDC “retirement pose” (Figure 1d) was designed to provide higher-resolution coverage of these two targets; once the IDC is no longer required for engineering purposes, it will be stowed in this retirement pose and will be used for change detection of primary targets over the duration of the mission (change detection images examined herein are not acquired from this retirement pose).

ICC images were also differenced in order to search for subtle variations in surface color caused by the redistribution of surface material. When this procedure yielded detection of linear darker-albedo tracks, we performed a more robust image differencing technique in order to quantitatively describe these tracks (e.g., track orientation, distance of closest approach, contrast). For every ICC image, we selected four preceding images that minimized expected differences, using a metric that balances differences in local time (i.e., illumination changes) with number of sols between images (i.e., changes in dust on the optics). Ratio images were then constructed, dividing the target image by each of the four preceding images, and normalizing by dividing by the mean value to remove bulk illumination changes. To facilitate visual detection of subtle albedo changes, images were displayed such that the full black-white range spanned ±10%. For images where such a track was detected, the contrast was measured at several places to find a peak contrast. The ratio image was then map-projected onto a flat surface parallel to the lander. The lander attitude was chosen to prioritize accuracy close to the lander; all measurements more than a few meters from the lander have projection errors that accumulate rapidly with distance. Within the map projection, distance from the camera, width, and track orientation were then measured.

2.2. Orbital Change Detection Imaging

We also use multitemporal images acquired by the Mars Reconnaissance Orbiter's High Resolution Imaging Science Experiment (HiRISE) camera (McEwan et al., 2007) between 2014 and 2020 (Figure 1b, Table S2, and Movie S4) to search for evidence of bedform migration in the region surrounding *Homestead hollow* (within a HiRISE footprint centered at InSight, typically within a few kilometers of the InSight lander). This high-resolution camera has a pixel scale of ~0.25 m/pixel (McEwan et al., 2007), and bedform migration can be confidently detected and measured with a 3-pixel change (equivalent to ~75 cm of motion). The HiRISE images used for orbital change detection analyses were ideal for change detection as they were acquired under similar conditions and with comparable camera roll angles (within ~10°). Map-projected images were overlaid and co-registered to immobile tie points (i.e., permanent surface features, fractures, and large rocks) and analyzed in ArcGIS for detection of changes over time. Bright albedo bedforms interior and immediately exterior to the craters, and darker sediment deposits interior to the craters (some with ripple-like morphologies), were investigated in multiple locations throughout the HiRISE image pair.

2.3. InSight Meteorological Data

The Auxiliary Payload Sensor Suite (APSS) instrument takes continuous measurements of wind speed and direction as well as atmospheric pressure and temperature (Banfield et al., 2018; Spiga et al., 2018). Winds and air temperature are measured by the dual-boom Temperature & Wind for InSight (TWINS) instrument at a height of 1.2 m above the surface, while pressure is measured by a very sensitive, fast-response pressure sensor (PS) inside the lander body. At the beginning of the mission (until Sol 145), TWINS and PS returned respectively 0.1 Hz and 1 Hz measurements by default, but higher frequency (1 Hz and up to 20 Hz) data could be downlinked for periods of interest (e.g., when wind-driven changes were observed or a pressure drop was detected). Since then, however, 1 Hz TWINS and 10 Hz PS data have been returned continuously except for rare periods when high-frequency data were lost. We examine the full APSS data set through Sol 400 of the mission in order to obtain a complete picture of the meteorology at the landing site and to characterize seasonal variability in circulation patterns and vortex activity. We also conduct more detailed assessment of atmospheric conditions on sols that contained sediment motion (and that were separated by ~45° of L_s to provide good coverage across the mission) in order to assess diurnal variability within seasonal regimes and to constrain the surface forces present during each observed change. When viewed in the context of all available data, these individual sols can help us understand the nature of ongoing aeolian surface modification at *Homestead hollow* and across the region.

2.4. Atmospheric Model Simulations of the Landing Site

Mars Weather Research and Forecasting (MarsWRF) is a multiscale model of the Martian atmosphere, described in Richardson et al. (2007), Toigo et al. (2012), Newman & Richardson (2015), and Newman et al. (2017, 2019). As described in detail in those papers, MarsWRF includes parameterizations of the CO_2 condensation-sublimation cycle, surface-atmosphere interactions, boundary layer mixing, and radiative transfer through the dusty Martian atmosphere. Topographic height is given by Mars Orbiter Laser Altimeter (MOLA) maps (Smith & Zuber, 1996), roughness using MOLA intrashot data (Garvin et al., 1999; Neumann et al., 2003), with albedo, thermal inertia, and emissivity derived from Mars Global Surveyor Thermal Emission Spectrometer (TES) observations (Putzig & Mellon, 2007). For this study, MarsWRF was run as a global 2° model with three "nested" higher resolution regions centered on InSight's landing site, with each nest smaller than its parent and at three times the horizontal resolution. This gives a model grid spacing of ~4.4 km in the innermost nest; as such, MarsWRF outputs are more representative of spatio-temporal averages, as the mesoscale grid spacing does not resolve local turbulence. The vertical grid used was grid A in Newman et al. (2017), which has three model layers below 150 m and thus finely resolves the lower boundary layer; however, results using grid B (which has its lowest layer at ~145 m) gave similar results, indicating far less sensitivity to this choice than found by Newman et al. (2017) in Gale crater.

The simulations conducted here used the KDM (k-distribution model) radiative transfer scheme (Mischna et al., 2012) with the atmospheric dust distribution imposed using the Mars Climate Database (MCD) Mars Global Surveyor (MGS) dust scenario, which represents a year without any major dust storms (Montmessin

et al., 2004). The exception is for a second simulation covering the period between L_s ~320 and 360°, when the effect of a regional dust storm in Mars Year (MY) 34 is included by basing the column dust opacity on the MY 34 dust maps of Montabone et al. (2020). This allows the impact of the storm on the local meteorology to be investigated and compared with the nondust-storm simulation results. Note that, while dust opacities at InSight over the entire mission period are available, the model requires the dust distribution to be specified over the entire globe, with several meteorological variables (e.g. wind and pressure) being more sensitive to the regional and global dust distribution than to local dust abundances. Future work will merge the local InSight measurements with regional dust opacities measured from orbit to create a map of column dust opacity that is both regionally and locally consistent with observations for the InSight mission, but that is beyond the scope of this work.

We use MarsWRF output to predict the DDA and tangential speed around a vortex core, following the scheme presented in Rennó et al. (1998). The DDA is defined as the flux of energy available to drive dust devils and is proportional to a function of the boundary layer thickness and to the sensible heat flux. In turn, the latter is proportional to the air density, drag velocity, surface-to-air temperature difference, and a drag coefficient which varies with the atmospheric stability. For full details of how the DDA is calculated inside MarsWRF, see Newman et al. (2019). The DDA is a measure of the energy that may be harnessed by vortices, but how this should be distributed into a vortex distribution is not clear at present (i.e., whether an increase in DDA results in more vortices or an increase in vortex strength or both). It is also possible that some threshold DDA must be exceeded for vortices of a given intensity (i.e. pressure drop magnitude) to occur, or for a vortex to raise dust from the surface (Newman et al., 2019). In this sense, the exact meaning of the DDA parameter is somewhat ambiguous, but can be used in a relative sense to examine seasonal and diurnal variability in vortex activity. Due to the ambiguity of this parameter, we compare DDA to both the number of detected vortices as well as the magnitude of the pressure drops recorded by APSS (Spiga et al., 2020 this issue). Atmospheric conditions (wind speed, wind direction, atmospheric pressure, temperature, DDA, and associated tangential velocities) were output from MarsWRF every minute over a full Mars year and were compared to the APSS data available from the first 400 sols. The peak tangential wind speed around the vortex core is calculated in Rennó et al. (1998) by assuming that dust devils are in cyclostrophic balance, thus the radial pressure drop across the vortex (which is estimated by the Rennó et al., 1998 scheme) can be used to derive the tangential wind speed at the vortex radius (the radius of maximum wind).

To summarize, we utilize outputs from the MarsWRF atmospheric model (e.g., pressure, temperature, and wind) to provide predictions of (i) peak mesoscale wind speeds, (ii) vortex properties using the theory of Rennó et al. (1998) (which relates them to local dynamical and thermal properties of the atmosphere and surface; see below), and (iii) particle motion (based on assumed wind stress and dust devil lifting thresholds). These predictions are compared with InSight observations of (i) peak in situ, 1 Hz wind speeds, (ii) vortex properties, and (iii) particle motion seen in imaging. The purpose of including model output is partly to provide a direct comparison with InSight wind data and determine whether the model (which cannot resolve shortlived wind gusts or vortices) can reproduce the temporal variation in magnitude and/or direction of wind. If the model is able to reproduce winds sampled by APSS, this provides greater confidence in our ability to extrapolate these results across the part of the year that has not yet been measured. Additionally, MarsWRF provides predictions of variables that cannot be measured directly from InSight are needed to calculate Rennó et al. (1998) vortex activity (e.g., sensible heat flux and PBL thickness).

2.5. Sediment Transport Models

In order to understand the nature of the aeolian activity at *Homestead hollow* (i.e., susceptible grain sizes, associated motion thresholds, and dominant surface forces), we consider three different models of sediment mobilization: traditional saltation (Shao & Lu, 2000); surface creep/rolling (Merrison et al., 2007); and vortex-induced lifting (Greeley & Iversen, 1985). Such a comprehensive assessment is particularly important given that on some sols there was evidence of concurrent motion of a wide range in particles between dust and granules and in other cases it was not possible to resolve the size of the mobilized grains at all (Charalambous et al., 2021, this issue). Thus, a robust analysis of observed wind-induced motion should consider all possible grain sizes and all possible modes of transport. We also explore the effect that

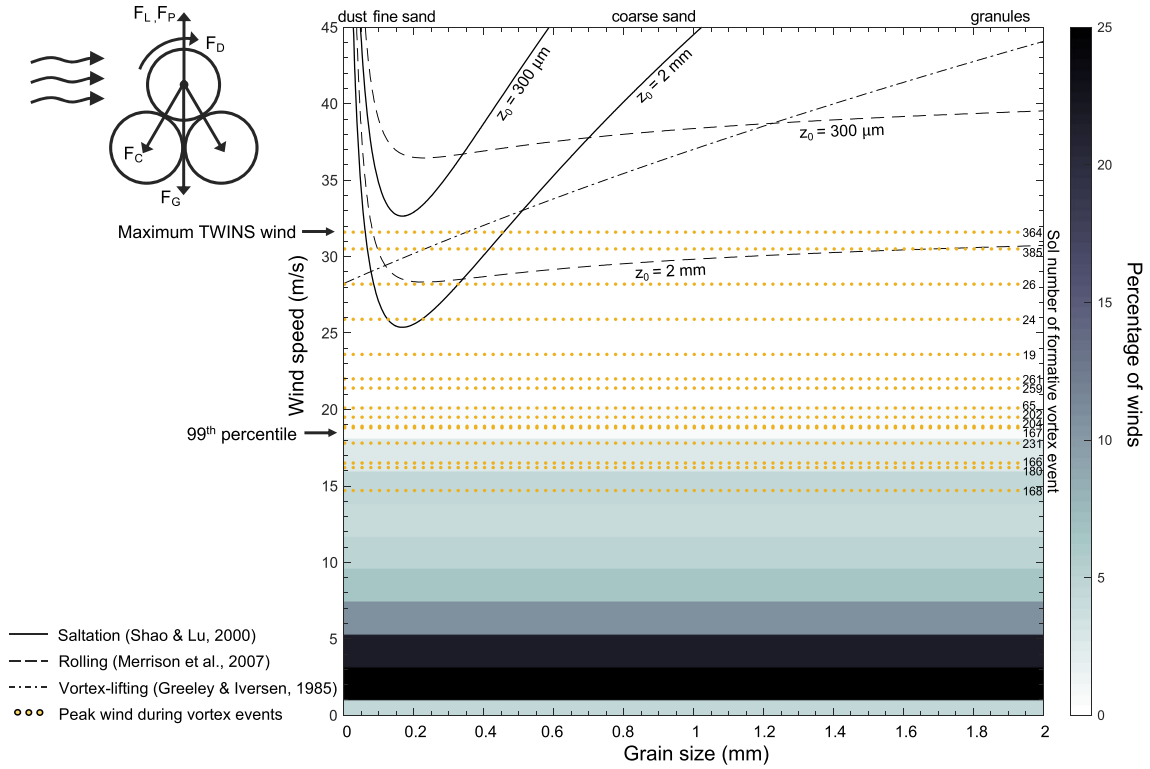

Figure 2. Distribution of TWINS wind speeds compared to fluid thresholds for saltation (Shao & Lu, 2000, Equation 1), drag-induced rolling (Merrison et al., 2007, Equation 3), and vortex lifting (Greeley & Iversen, 1985, Equation 5) using a range of z_0 between 300 μm and 2 mm. Only 0.06% of winds measured thus far since landing have exceeded the minimum threshold identified by either of these models, consistent with low levels of surface activity. The schematic in the top left shows the forces that might act on an individual particle during a convective event based on a combination the models examined herein (gravitational force, F_G; interparticle cohesive forces, F_C; horizontal drag force, F_D; drag-induced lift force, F_L; and vertical pressure force, F_P). Subset grain diagrams included within the threshold plot indicate the hypothesized modes of transport for and dominant mobilizing forces acting on dust, sand, and granules based on observed motion, atmospheric conditions measured by APSS, and threshold wind speeds are listed in Table 1. APSS, Auxiliary Payload Sensor Suite; TWINS, Temperature & Wind for InSight.

variations in atmospheric density have on anticipated motion thresholds, a factor that is rarely considered in aeolian research but may play a more important role in wind-driven transport on Mars than on Earth.

In general, wind can produce aeolian surface activity when the erosive forces acting on a particle are strong enough to overcome stabilizing forces; the specific mode of transport that occurs with mobilization (e.g., suspension, saltation, or surface creep) depends on both the material properties (e.g., grain size D_p, density ρ_p, and cohesion) and environmental conditions (e.g., wind shear stress τ, atmospheric density ρ_a and gravity g). Traditional wind tunnel experiments (Bagnold, 1941; Greeley et al., 1980) have generally focused on saltation of sand particles, as this is the dominant mechanism guiding the development of aeolian bedforms (dunes and ripples). In this scenario, the major stabilizing forces are considered to be gravity and interparticle cohe sive forces and the major erosional force is the horizontal drag force generated by the shear stress resulting from boundary layer winds flowing over the surface (Figure 2). Saltation thus occurs when the wind friction velocity (defined as $u_* = \sqrt{\tau \rho_a}$; e.g., Stull, 1988; White, 2006) exceeds a critical value termed the "fluid threshold"; an elegant model for the fluid threshold friction speed was presented in Shao and Lu (2000):

$$u_{th} = \sqrt{A_N \left(\sigma_p g D_p + \frac{\gamma}{\rho_a D_p} \right)} \quad (1)$$

In this equation, A_N and γ are empirically derived constants of 0.0123 and ~3×10^{-4} kg/s^2, respectively, and σ_p is the ratio between particle and atmospheric density $\left(\frac{\rho_p}{\rho_a}\right)$. Equation 1 is a modification of the original threshold equation presented in Bagnold (1941), and it is perhaps the most commonly used expression for predicting aeolian activity on Mars.

Even though shear stress is the more fundamental parameter controlling sediment motion than friction speed, studies typically cite the corresponding friction speeds, as variations in atmospheric density are assumed to be negligible on Earth. This is not the case on Mars, however, where there are large seasonal and diurnal variations in atmospheric density, making it nontrivial to convert shear stress to a single friction speed. The continuous wind speed and pressure data provided by the APSS instrument provide an opportunity to calculate exact surface shear stresses and explore the impact that changes in atmospheric density have on aeolian activity. With this in mind, we can use Equation 1 to solve for a single threshold shear stress, which is independent of atmospheric density:

$$\tau_{th} = A_N\left(\rho_p g D_p + \frac{\gamma}{D_p}\right) \tag{2}$$

Based on this relation, we calculate the minimum threshold shear stress for the most-readily mobilized material (~150 μm sand) to be 0.045 Pa. We can use this value to examine the difference between aeolian activity predicted using traditional u_{th} values (assuming an average atmospheric density) and using τ_{th}.

It is also important to note that Equation 1 is most appropriate for the idealized scenario of steady-state saltation within unimodal aeolian bedforms (i.e., ripples and dunes), which is not representative of all naturally occurring surfaces or transport modes. In order to assess the possibility of surface creep, we also utilize the model put forward by Merrison et al., 2007, which incorporates the impact of direct drag-induced rolling:

$$u_{roll} = \left(\frac{\frac{\pi}{6} g \rho_p D_p^3 + C_{adh} D_p}{\left(C_L D_p^{2-n} + C_D D_p^{3-n}\right)\rho_a^{1-n}}\right)^{1/(2-n)} \tag{3}$$

where coefficients C_{adh}, C_L, C_D, and n were, respectively, determined to be 2.7×10^{-5} N/m, 1.45, 4.4×10^4 m^{-1}, and 0.07 for spherical glass beads. Although the experimental setup used to derive this equation may not be perfectly analogous to the surface at the landing site, to our knowledge this is the most robust model that has been put forward to quantify the winds required for surface creep and it has been successfully applied to aeolian transport on Mars previously (Baker et al., 2018a; Bridges et al., 2017).

The fluid thresholds calculated from Equations 1 and 3 can be used to extrapolate a freestream wind speed at the equivalent height of the TWINS booms ($z = 1.2$ m) using the logarithmic "Law of the Wall" (e.g., Kok et al., 2012):

$$V(z) = \frac{u_*}{\kappa}\ln\left(\frac{z}{z_0}\right) \tag{4}$$

where κ is von Karman's constant (~0.4) and z_0 is the aerodynamic surface roughness, which represents the height at which the wind speed profile goes to zero. The value of z_0 is generally controlled by the size and spacing of nonerodible surface elements that impact the wind profile close to the surface. In reality, z_0 can only be accurately determined through wind speed measurements made at two different heights above the surface (z_0 has only been directly measured once on the surface of Mars from Mars Pathfinder, which had windsocks at different heights on the mast; see Sullivan et al., 2000) but more commonly it is estimated through assessment of the surface particles in the direct vicinity of the spacecraft. As there is significant uncertainty in these values, we have chosen to apply a range of possible aerodynamic surface roughnesses (300 μm–2 mm), which were derived by applying local rock abundances to the Hebrard et al., 2012 surface roughness model (see Charalambous et al., 2021 for further explanation of surface roughness estimates).

Whereas Equations 1 and 2 are useful for understanding the dynamics of motion as a result of freestream boundary layer winds, they are less useful for understanding mobilization of sediment during convective events, which are significantly more complicated. In particular, vortex flow introduces additional surface forces that are not considered in traditional fluid threshold equations (e.g., the vertical pressure gradient and electrostatic forces). A limited number of studies have sought to quantify the impact of the pressure gradient on sediment lifting, and even fewer have derived a formula for use in these situations (see review by Neakrase et al., 2016). However, assuming vortices are in cyclostrophic balance allows one to approximately relate the pressure drop across the vortex with the maximum tangential velocity. Greeley and Iversen (1985) used this approximation to derive an empirical formula for the threshold tangential wind speed required to entrain sediment during a convective event:

$$V_{\tan}^{t} = \left(1 + \frac{150}{\rho_d g D_p}\right)^{1/2} \left(\frac{\rho_d g D_p}{\rho_a}\right)^{1/2} \tag{5}$$

Note that while this threshold is formulated in terms of the peak wind speed around the vortex core, it is intended to account for additional processes acting to raise dust rather than the wind stress effect alone, because the physics of vortex dynamics relate the tangential wind speed to the pressure drop and more. Part 1 introduces some of these vortex-specific effects and explores their possible interactions as the vortex passes by the station; here we more robustly analyze how the unique conditions with a vortex can enhance sediment transport. Although all threshold equations should be considered with caution (their limitations are discussed more in Section 4), they can provide valuable insight into the physics of grain transport and help elucidate the dominant surface forces controlling mobilization of different size populations. Although Equation 5 is not formulated as a friction speed, it is similarly dependent on atmospheric density, and thus we can also examine the role that seasonal variations in atmospheric density have on this threshold. Figure 2 shows the threshold curves for the three transport models described herein for average atmospheric density (~0.019 kg/m^3), which is useful for determining probable modes of transport for a range of grain sizes. Figure 7 considers the effect of seasonal variations in atmospheric density on these thresholds.

3. Results

Overall, the surface at Homestead hollow has been generally stable over the first 400 sols of the mission, with localized aeolian motion observed on the surface and within disturbed sediment piles (Part 1; Charalambous et al., 2021, this issue). Fifteen instances of localized surface change were observed over this timeframe (indicated with yellow lines in Figure 3 and summarized in Table 1, which is adapted from Part 1). Between Sol 18 and 65, fine material (<62 μm; Charalambous et al., 2021, this issue) was incrementally removed from the lander footpad (Movie S1); ICC images captured four distinct removal events, and higher-resolution IDC images acquired on Sol 10 and 106 were used to confirm this removal. On multiple sols, ICC image differencing also revealed the formation of linear darker-albedo features resembling dust devil tracks in the vicinity of the lander (Figure 5, Table 2); these subtle surface color changes are likely caused by the removal or redistribution of fine surface material. Some localized (non-linear) surface color changes were also apparent without image differencing (Movie S2), which may similarly be caused by redistribution of surface dust. Opportunistic IDC images acquired while the scoop was positioned only ~0.65 m above the surface (Figure 1c) were able to capture sporadic creep of granules up to 3 mm in diameter on Sol 364 and Sol 385 (Movie S3; Charalambous et al., 2021, this issue). Although these four types of motion were categorized differently (i.e., footpad changes, dust devil tracks, surface darkening, and granule creep), we hypothesize that they likely do not result from distinct atmospheric phenomenon; on many sols, two or more types of change occurred concurrently (Table 1) and all seem to correspond to the passage of convective vortices detected in APSS data by abrupt drops in atmospheric pressure and simultaneous increases in wind speed (Figure 5). The candidate convective events associated with each observed change are reported in Part 1 (Charalambous et al., 2021) and are summarized in Table 1.

While the timing of observed changes generally correlates with expected seasonal and diurnal variations in vortex activity and wind (enhanced vortex activity and higher wind speeds occur during midday of local

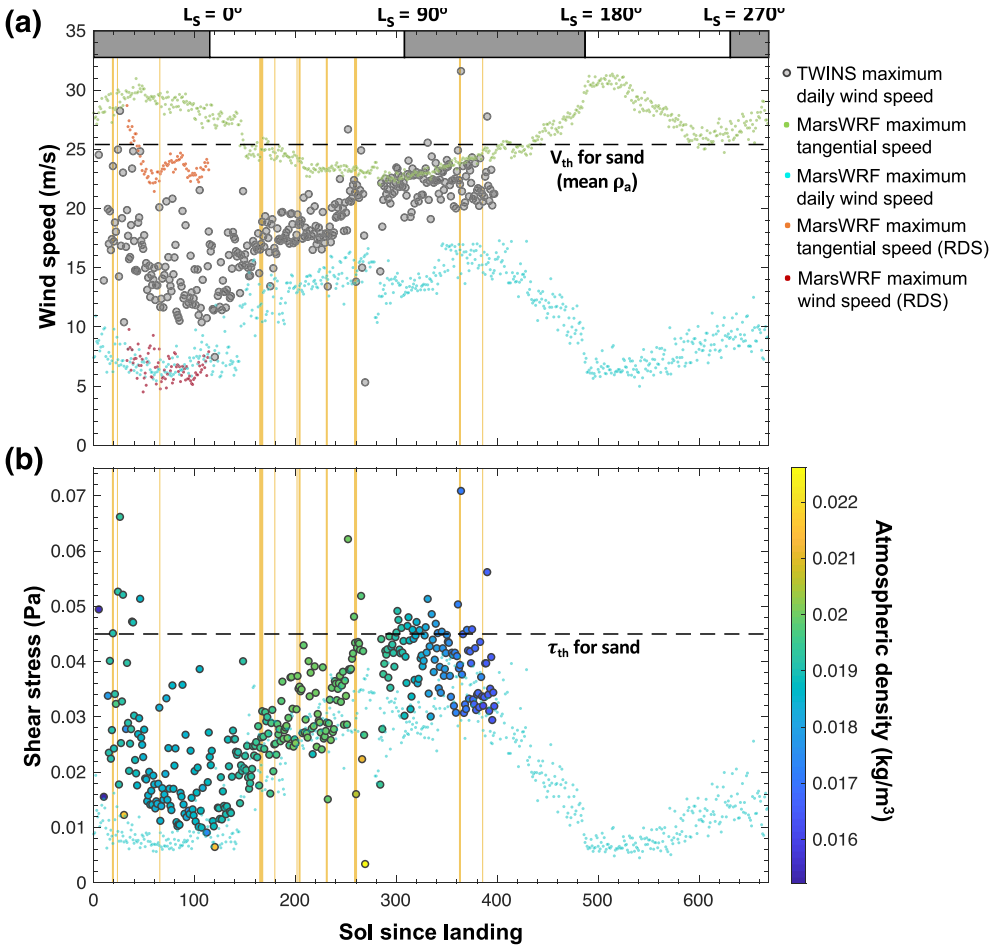

Figure 3. (a) Seasonal variability in maximum daily wind speed recorded by TWINS (gray circles) compared to MarsWRF predictions for maximum freestream winds (blue dots) and maximum tangential velocity (green dots). Maximum freestream winds and tangential speed are also simulated through $L_s = 0$ for the regional dust storm (red and orange dots, respectively). The anticipated minimum threshold velocity for sand (dashed line) is calculated using Equations 1 and 4 and $z_0 = 2$ mm. (b) Seasonal variability in maximum shear stress measured by APSS (circles) color-coded by atmospheric density (again calculated using $z_0 = 5$ mm) compared against MarsWRF predictions for shear stress (blue dots) and the critical shear stress for saltation of sand (dashed line). Sols with surface change are noted by the yellow lines. APSS, Auxiliary Payload Sensor Suite; MarsWRF, Mars Weather Research and Forecasting; TWINS, Temperature & Wind for InSight.

spring and summer), aeolian activity is stochastic in nature, as some particularly energetic events (as indicated by high winds and/or large pressure drops) did not produce any observable motion (Figures 3 and 4). The implications of this are discussed further in Section 4. We compare seasonal variations in peak daily measured winds (wind speed at 1.2 m and shear stress at the surface) as well vortex activity recorded by APSS to MarsWRF wind, shear stress, and DDA predictions. For completeness, we compare the daily maximum wind speed measured by TWINS to MarsWRF predictions of both daily maximum freestream wind speed and the maximum tangential speed predicted around a vortex (Figure 3a) as vortex-induced gusts cannot be captured explicitly in a mesoscale model; a much finer model resolution, with grid spacings of ~10m, would be required to resolve vortices. Although the overall shape of the MarsWRF freestream wind curve provides a better fit to the seasonal variation in peak measured winds, predicted tangential speeds do a better job at matching the actual wind speeds measured on the surface.

As the physical representation of predicted dust devil activity (DDA) is somewhat ambiguous, we compare MarsWRF DDA to both the number and magnitude of pressure drops recorded by APSS (Figures 4a and 4b). Again, a MarsWRF simulation including the regional dust storm seems to better simulate the signif-

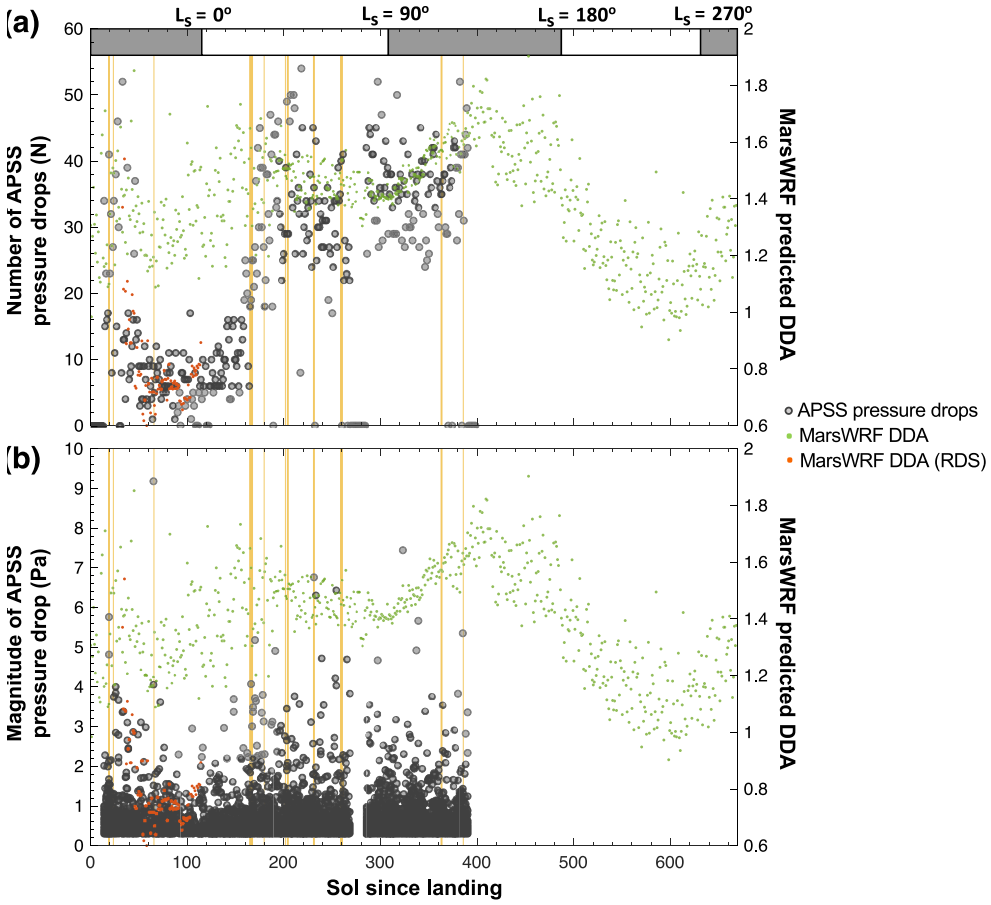

Figure 4. (a) Number of pressure drops detected in APSS data every sol (gray circles) compared against MarsWRF predictions for dust devil activity during "normal" conditions (green dots) and including the regional dust storm through $L_s = 0$ (orange dots). (b) The magnitude of pressure drops recorded by APSS (gray circles) compared against MarsWRF predictions for dust devil activity during "normal" conditions (green dots) and including the regional dust storm through $L_s = 0$ (orange dots). Sols with surface change are noted by the yellow lines; aeolian activity displays some seasonality corresponding to periods of higher winds and larger pressure drops associated with enhanced vortex activity, but motion is also found to be stochastic, as some particularly high winds and large pressure drops did not correlate with any observable surface change. APSS, Auxiliary Payload Sensor Suite; MarsWRF, Mars Weather Research and Forecasting.

icant decrease in DDA at the end of winter. It is interesting to note that MarsWRF DDA peaks earlier in the year (L_s ~140°) than tangential speed (~L_s 200°). This is because DDA is proportional to sensible heat flux and vertical thermodynamic efficiency, whereas the tangential wind speed depends only on the size of the pressure drop, which depends in turn on the thermodynamics of the convective plume. Thus, while predicted DDA is directly related to wind speed via the drag velocity term in the sensible heat flux equation, the predicted tangential wind speed is not. While the most appropriate formulation of the DDA is still to be determined, it is possible that a 'wind speed' effect may be present in observations anyway, due to stronger winds blowing more vortices over a stationary sensor in the same period (as opposed to stronger winds causing more vortices to be present in a given area). Continued monitoring over the rest of the Mars year will help constrain the seasonal variability in environmental conditions and resultant surface activity and determine which MarsWRF parameters (i.e., freestream winds, tangential speed, DDA) are most useful for predicting vortex-induced sediment motion. It is worth noting that a regional dust storm occurred shortly after landing, greatly increasing atmospheric dust levels and thus decreasing solar insolation and the drive for convection. Results from a MarsWRF simulation run with the dust storm included up until $L_s = 0°$), using observed dust column opacities to impose dust loading in the model, are also shown in Figure 3. The tangential wind speeds predicted by this simulation show a better match to the observed seasonal variations

Table 1
Summary of Surface Changes Observed During the First 400 Sols of the InSight Mission

Time 1	Time 2	Candidate event	Wind speed (m/s)	Pressure drop (Pa)	Type
Sol 18 13:38	Sol 20 13:03	Sol 19 14:08	23.6	5.8	Footpad, DD track
Sol 23 14:12	Sol 24 13:04	Sol 24 12:14	25.9	3.7	Footpad
Sol 26 11:03	Sol 26 15:53	Sol 26 13:47	28.2	4	Footpad
Sol 65 13:48	Sol 66 10:05	Sol 65 13:32	20.1	9.2	Footpad
Sol 164 16:41	Sol 166 16:41	Sol 166 12:50	16.5[a]	4	DD track
Sol 166 16:41	Sol 167 16:20	Sol 167 11:46	18.8	3	DD track
Sol 167 16:20	Sol 168 16:18	Sol 168 11:34	14.7	3.5	Surface darkening
Sol 179 16:31	Sol 180 16:31	Sol 180 12:16	16.2	2.3	DD track
Sol 201 17:23	Sol 202 16:41	Sol 202 12:52	19.5	1.2	DD track
Sol 203 13:46	Sol 205 13:26	Sol 204 10:42	18.9	2.1	DD track
Sol 230 17:31	Sol 232 13:18	Sol 231 12:36[b]	17.8	6.8	DD track, surface darkening
Sol 258 16:33	Sol 259 13:11	Sol 259 10:51[c]	17.7	1	DD track
		Sol 259 11:32[c]	21.4	0.7	
Sol 259 13:11	Sol 261 15:31	Sol 261 11:55	21.3	2.3	DD track
Sol 362 15:54	Sol 364 15:54	Sol 364 13:28	31.6	3.5	Granule creep
Sol 385 11:56	Sol 385 15:54	Sol 385 12:33	30.5	5.4	Granule creep, saltation, DD track

Note. Adapted From Part 1 (Charalambous et al., 2021, This Issue).
[a]The maximum wind speed on Sol 166 was 17.1 m/s, but this peak wind was not accompanied by a pressure drop, and thus was not selected as the formative event. [b]Gata gap on Sol 232 between 00:00 and 15:13. [c]Two candidate events were identified during this timeframe with moderately strong winds and small pressure drops.

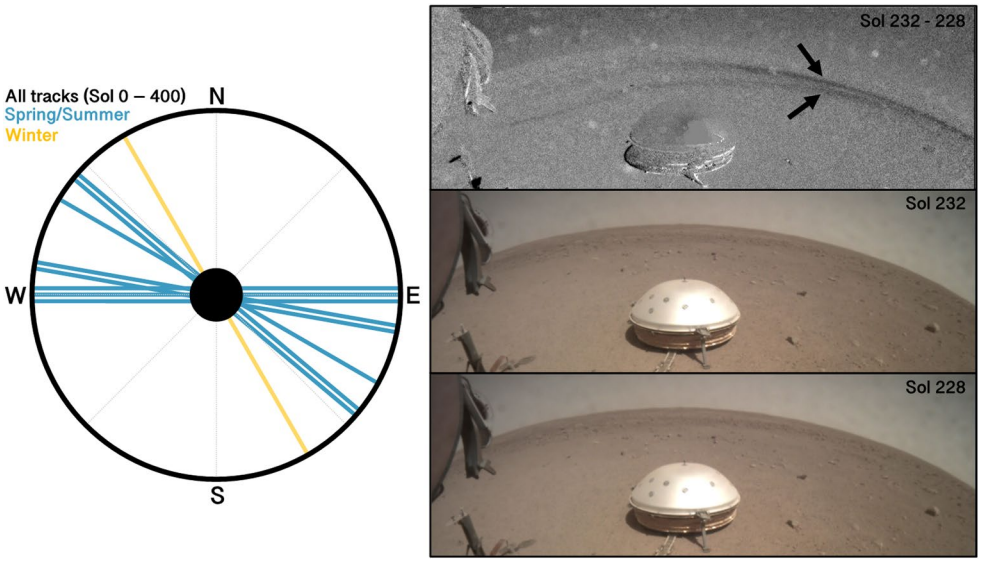

Figure 5. Left: orientation of all dust devil tracks observed in ICC images between Sol 0 and 400. Tracks are primarily oriented NW-SE, consistent with those seen from orbit (Reiss & Lorenz, 2016; Perrin et al., 2020, this issue) and seasonally reversing winds (Banfield et al., 2020). Tracks formed in the winter are driven by dominant northwesterly winds (yellow), and spring and summer tracks are driven by southeasterly winds (blue). The uncertainty in track azimuth angle increases with increasing distance from lander (see Table S1 for track distances). Right: Example of ICC image differencing method for track detection. ICC, Instrument Context Camera.

Table 2
Dust Devil Track Parameters Measured in ICC Images.

Sol	Closest approach (m)	Closest approach (°)	Azimuth (°)	Width (m)	Peak contrast (%)
19	13	180	150	2	3
166	6	220	90	2	<1
167	3	230	130	0.5	2
180	3.5	220	120	0.5	<1
203	13	190	100	2	3
231	7	180	90	2	4
259	2.7	220	130	0.3	4
261	11	180	90	2	3
385	3.5	200	130	3–5	2

Tracks are generally oriented northwest-southeast (North is 0°).

in peak wind speed, due to the decreased convective activity during the storm.

According to the transport models used herein, the minimum theoretical wind speed required to mobilize sediment at the InSight landing site is ~25 m/s, assuming an average atmospheric density = 0.019 kg/m^3 and maximum z_0 = 2 mm (Figure 2). Approximately 1% of the daily peak winds exceed this threshold, but this is equivalent to less than 0.001% of winds measured since landing overall and is consistent with the generally low levels of observed aeolian activity. Of the fifteen vortices hypothesized to be responsible for the observed changes, only four had peak measured wind speeds exceeding this value, and conversely, not all winds above this value produced observable changes. Whereas the threshold curves in Figure 2 should be considered with caution, comparison between these differing transport models can help interpret the simultaneous movement of a wide range in grain sizes observed during vortex encounters and illuminate the relevant surface forces acting on different size populations (see Section 4 for more discussion). Based on these formula, in the presence of a convective vortex, similar wind speeds may be able to mobilize a range of grain sizes from dust to granules, consistent with observed motion. That said, it is notable that ~75% of peak winds measured during formative vortex events are below the minimum threshold of 25 m/s predicted by Shao and Lu (2000) for entrainment of ~150 μm sand. Based on Equation 1 (which is commonly applied to aeolian activity on Mars), both smaller and larger particles require higher winds to be mobilized by boundary layer winds; granules would require roughly double the wind speeds, while dust would require roughly four times higher winds. Instead, direct dust entrainment could be achieved at similar speeds to mobilization of sand if one considers the additional lift provided by the vertical pressure gradient at the center of the vortex (Equation 5); this delta-P effect is most effective on fine dust particles, hence why the left side of the Greeley and Iversen (1985) curve is significantly reduced from the traditional Shao and Lu (2000) curve. At the coarse end of the grain size range, the Merrison et al. (2007) model (Equation 3) indicates that granules can roll across the surface at lower winds than would be predicted by Shao & Lu, 2000 for lifting off the bed (and at wind speeds more equivalent to those required for saltation of fine sand). In other words, whereas traditional threshold equations (e.g., Shao & Lu, 2000) are designed for saltation occurring in response to steady boundary layer winds, the other two models consider slightly different modes of transport (i.e., vortex-lifting and drag-induced rolling). Comprehensively, these three models can help us understand the dynamics of transport across a range of grain sizes.

In all seasons observed thus far, periods of enhanced wind are typically associated with daytime thermally-driven turbulence and peak wind gusts often correspond directly to the passage of a convective vortex above or near the lander. The highest wind speed measured during one of these convective events occurred on Sol 364 (31.6 m/s wind, 3.5 Pa drop) and the largest pressure drop occurred on Sol 65 (9.2 Pa drop, 20.1 m/s wind); both of these vortices generated sediment motion on the surface and the latter includes the largest pressure drop recorded on Mars to date (representing a ~1.2% drop in atmospheric pressure). Figure 6 shows the abrupt pressure drops and transient wind gusts that induced sediment motion on Sol 26 (removal of material on footpad) and on Sol 385 (surface creep and dust devil track formation). These two events are particularly useful given that they caused surface changes close to the lander (i.e., in the immediate workspace < 2 m away), so we have much better constraint on the grain sizes that were mobilized during these events (whereas the size populations being mobilized along more distant dust devil tracks is not well-constrained). In other words, the proximity between the location of sediment motion during these events and lander instruments (APSS, ICC, and IDC) allow us to more confidently correlate meteorological data with observed motion. Peak winds during both of these events were above the minimum predicted threshold of 25 m/s (Figure 6), but these wind gusts were short-lived; in the five-minute timeframe surrounding vortex encounters, winds demonstrate considerable variability in speed, indicating the transient and highly turbulent nature of convective events. Despite formative vortices being some of the most energetic events detected on the Martian surface to date, these vortices seem to be producing very limited sediment motion relative to those observed at some other landing sites. In Section 4, we analyze this

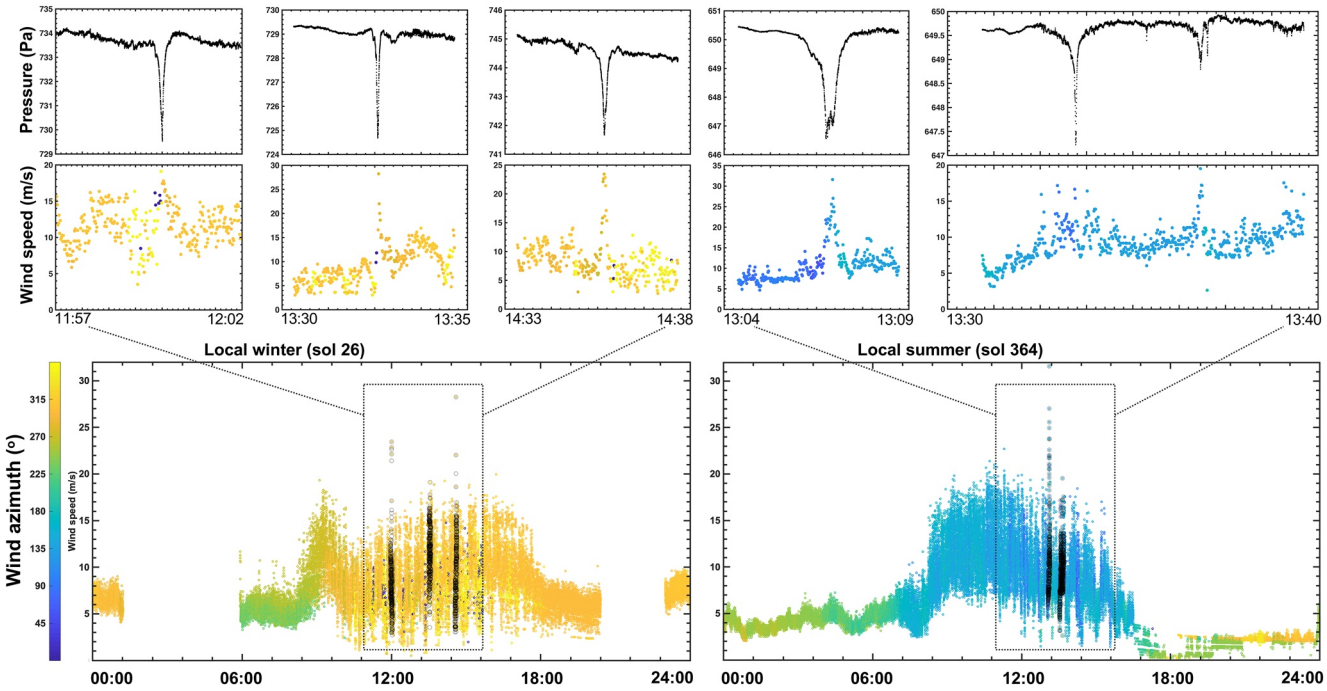

Figure 6. Two sols with energetic vortex encounters that resulted in sediment motion in the near workspace of the lander (Sol 26 and Sol 364). Peak wind speeds on both sols correspond to abrupt drops in atmospheric pressure and changes in wind direction, indicative of passing convective vortices. Vortices cause significant atmospheric turbulence; the 5 min around each convective event show considerable variability in wind speeds, and peak wind gusts are short-lived. Winter vortices are driven by northwesterly winds, while summer vortices are driven by southeasterly winds, consistent with the orientation of dust devil tracks seen in ICC images and from orbit. ICC, Instrument Context Camera.

finding in light of other lander and orbiter studies regarding dust devil activity and track formation in the region around *Homestead hollow*.

Figure 7 shows how these individual events fit into the overarching circulation patterns at this location: when the spacecraft landed during local winter, measured winds were predominantly northwesterlies. As spring approached, winds weakened overall and rotated 360° within each diurnal cycle. In late spring and summer, daytime winds strengthened again, this time showing a dominant southeasterly component. Nighttime winds are generally low across all seasons; daytime winds are particularly strong during summer. Comparison between MarsWRF output (Figures 3, 4, and 8) and APSS data (Figures 6 and 7) demonstrate that the model does relatively well at simulating seasonal and diurnal variability in wind speed over the part of the year sampled thus far. Although MarsWRF consistently underpredicts peak wind speeds, it accurately predicts the direction and time of peak winds. Daytime circulation patterns during winter (summer) are dominated by regional-scale northwesterlies (southeasterlies), which control the translational movement of vortices and thus the orientation of tracks formed in their wake. As atmospheric density varies across the first 400 sols of the mission, threshold wind speeds also vary accordingly by ~2–3 m/s, with the lowest (highest) thresholds occurring during local spring (summer). Although these variations may seem trivial, they do represent a ~10% uncertainty in traditional threshold estimates and a thorough investigation of these factors is vital when attempting to constrain motion thresholds on another planet. When maximum speeds are converted into wind stress using atmospheric density measurements (Figure 3b), even fewer wind gusts reach the minimum shear stress threshold of 0.045 Pa. This is particularly true in late spring and early summer, when atmospheric density is relatively lower.

Orbital HiRISE images over the landing site and immediately surrounding area, covering a time period of three Mars years (5.6 Earth years), did not reveal any clear evidence of bedform migration (Supplemental Movie S4). It is possible that the bedforms are moving at a rate below the HiRISE detection limit which is the time interval between repeat image acquisition combined with the resolution of the images (i.e., the bedforms have migrated a distance that is less than ~3 pixels, which in most cases is less than ~75 cm,

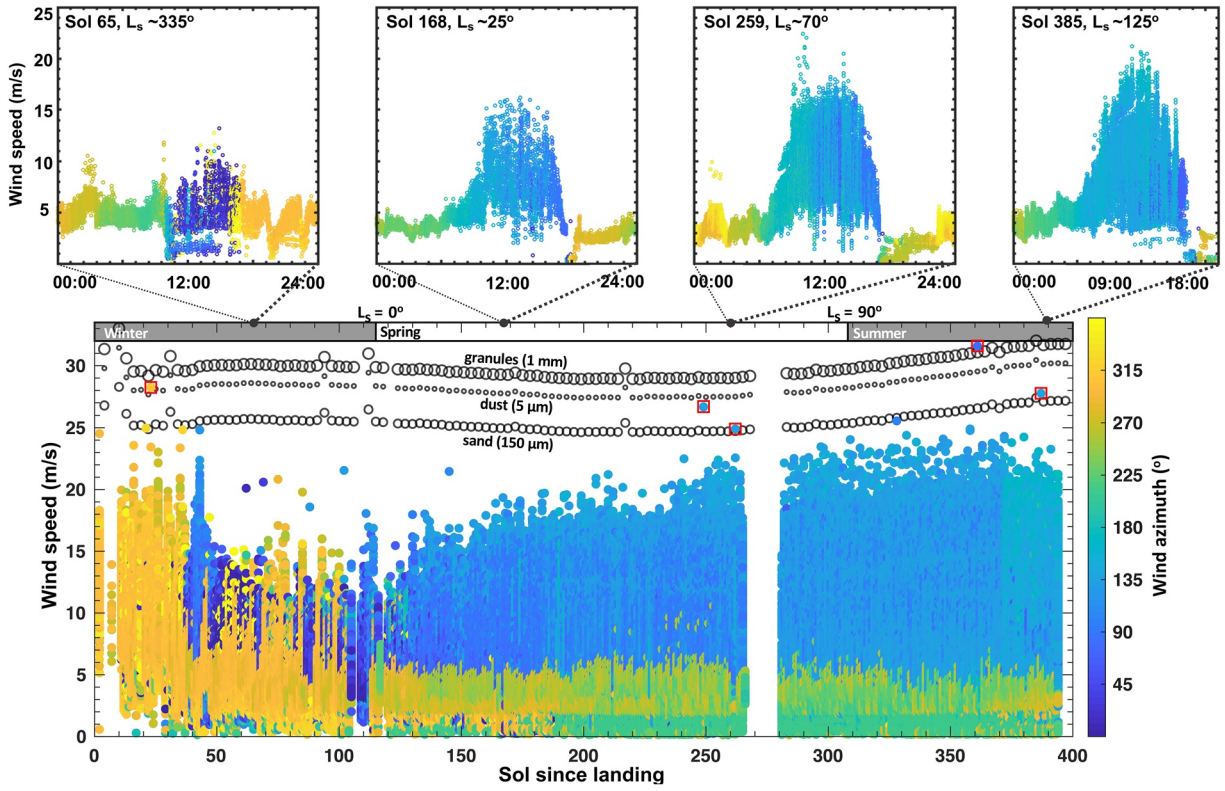

Figure 7. Wind speeds and directions as measured by TWINS across the full mission and for four sols that contained aeolian motion. Immediately after landing, circulation was dominated by northwesterlies that transition at the end of winter to strong southeasterlies in spring and summer (a regional dust storm at the end of winter may have suppressed wind strength). Winds are generally low at night in all seasons and peak winds generally occur in the middle of the day (between 10:00 and 15:00). Still, only a small percentage of winds exceed the minimum threshold wind speeds required for mobilizing dust (based on Equation 5), sand (based on Equation 1), and granules (based on Equation 3), each of which vary by ~2–3 m/s across the mission as atmospheric density changes. The sampled winds above at least one of the three thresholds are marked with a red box. TWINS, Temperature & Wind for InSight.

over the baseline). With this in mind, we can estimate an upper limit migration rate, based on the HiRISE detection limit, of ~0.15 m/Eyr (Earth year). Still, the lack of motion in aeolian bedforms over the observation window (and appearance of new dust devil tracks over that same period) is consistent with the lander observations of turbulent, low-flux changes caused by passing vortices and the lack of strong, sustained freestream winds necessary for the development and migration of aeolian bedforms.

4. Discussion

Robotic exploration of Mars has enabled the first observations of active aeolian transport on a planet other than Earth. As data continue to be returned from orbiting and landed spacecraft, researchers are able to build a more comprehensive understanding of aeolian surface modification across a wider range of environmental conditions. Of particular interest on both planets is establishing a robust understanding of critical motion thresholds, as this is a key parameter in predicting dune migration, estimating erosion rates, modeling dust activity, and mitigating risk to instruments. Extrapolating the most widely used terrestrial threshold model (Shao & Lu, 2000) to martian surface conditions implies that winds have to be an order magnitude of higher on Mars than on Earth to mobilize equivalent surface material. This threshold expression displays a nonlinear dependence on grain size with a minimum at ~150 μm, indicating that fine sand should be the most susceptible to wind-driven transport. Yet, currently available data suggest that contemporary martian winds rarely exceed these minimum thresholds, much less the significantly higher thresholds required to explain motion of both finer and coarser material. In other words, whereas sand transport on Mars is difficult to explain, it appears even more challenging to reconcile dust and granule motion with traditionally cited threshold values. This long-standing paradox has challenged our understanding of – and

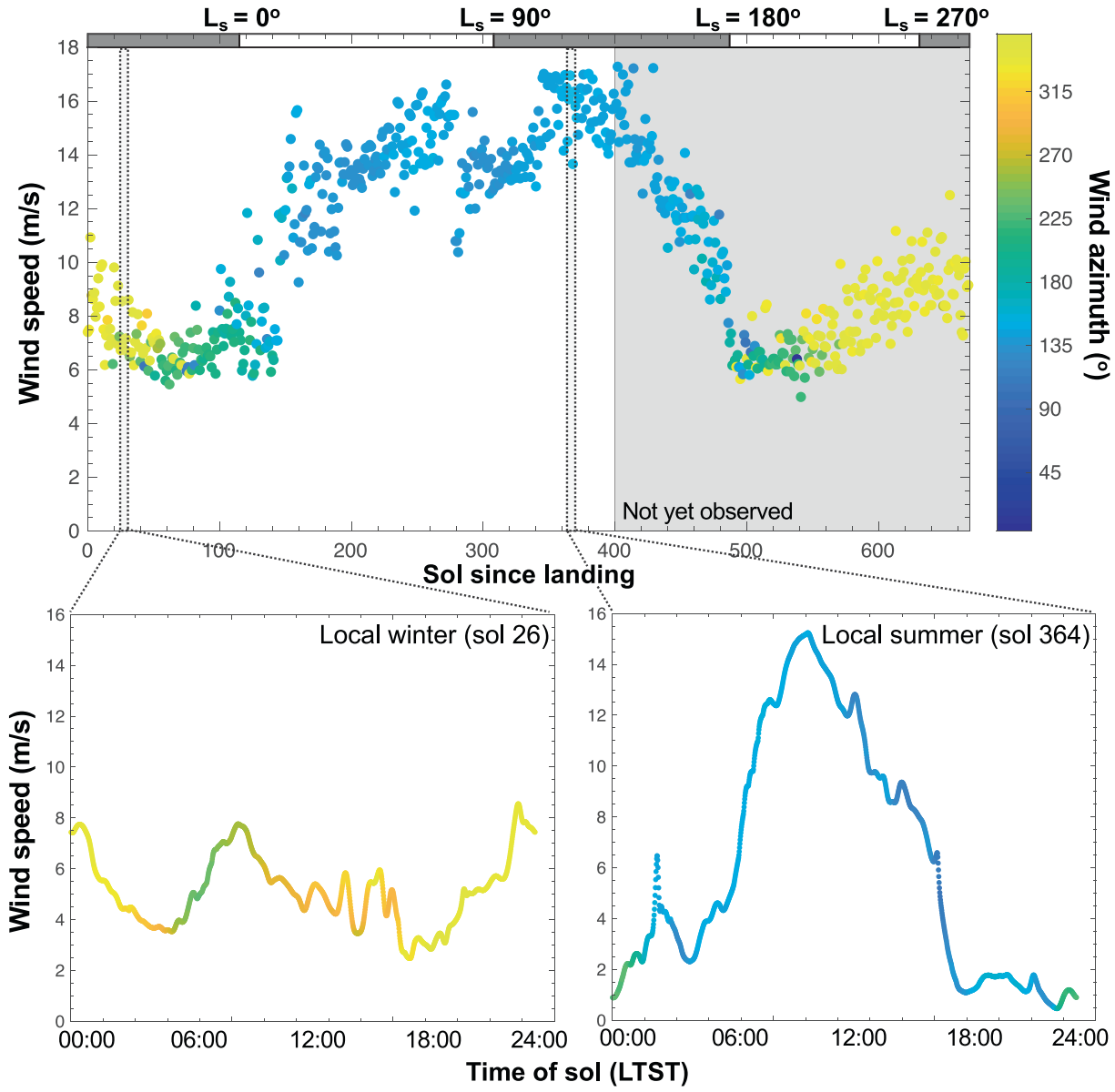

Figure 8. Seasonal and diurnal variability in peak wind speed and direction predicted by MarsWRF. Dominant winter (summer) circulation patterns are predicted to be controlled by regional-scale northwesterlies (southeasterlies), consistent with meteorological data presented in Figures 6 and 7. MarsWRF, Mars Weather Research and Forecasting.

thus ability to model – aeolian activity on Mars. Even on Earth transport models often fall short in their ability to explain aeolian activity observed in the field (e.g., Barchyn et al., 2014; Sherman et al., 1998), in large part due to inherent differences between controlled (and often idealized) experimental designs and the naturally turbulent conditions that exist within atmospheric boundary layers. For example, fluid thresholds have traditionally been derived for fully-developed saltation of unimodal sand within a steady wind flow. Yet, in reality, this set-up is not representative of most natural aeolian environments, where there are significant spatiotemporal variations in wind (and thus in resultant fluxes; see Baas & Sherman, 2006; Dupont et al., 2013; Stout & Zobeck, 1997) and where surface heterogeneities (e.g., in particle size, the distribution of nonerodible roughness elements, and moisture content) complicate the use of a singular deterministic threshold value for predicting erosion (Schönfeldt, 2004; Sullivan & Kok, 2017). Furthermore, atmospheric boundary layers in nature are ~10–100 times thicker than artificially imposed wind tunnel boundary layers,

which may introduce fundamental differences in turbulence and ensuing sediment mobilization (Pähtz et al., 2018).

The challenges associated with modeling aeolian activity from a set of simplistic, empirically-derived formulas are expounded when extrapolating to another planet. Recent advances in experimental and numerical modeling have revealed unexpected differences between martian and terrestrial saltation due to, for example, differing gravity on the two planets. Although gravity is explicitly considered in the Shao and Lu (2000) expression, it is difficult to quantify the complete influence gravity has on the initiation (and continuation) of sediment transport. Along with reducing the effective particle weight, the lower gravity on Mars may also impact sediment compaction (Musiolik et al., 2018) and particle trajectories (e.g., Almeida et al., 2008), thus facilitating saltation at lower friction speeds than are predicted by Shao and Lu (2000) (Sullivan & Kok, 2017; Swann et al., 2020). However, just as terrestrial field work is used to validate models on Earth, in situ data from the Martian surface are necessary to test these hypotheses and determine realistic motion thresholds. The joint imaging and high-frequency meteorological capabilities of the InSight lander provide a rare opportunity to correlate aeolian activity with atmospheric conditions on the surface. Here we take advantage of this opportunity to compare synchronous observational and meteorological data against activity predicted by three transport models in order to: (1) test the ability of current threshold equations to explain motion, (2) probe the dynamics of transport during erosional events, and (3) interpret the nature of ongoing aeolian modification at *Homestead hollow*. As each of the models presented herein was designed for use under slightly different conditions, integrating all three allows us to consider a wider range of possible transport modes. Whereas deterministic use of any one of these models should still be carefully considered given the inherently limited conditions under which they were derived, they are nonetheless still valuable for illuminating the dynamics of sediment transport occurring under on modern-day Mars.

Change detection images acquired since landing have revealed a highly stable surface surrounding the InSight spacecraft; minor surface erosion occurred during fifteen individual vortex encounters, as indicated by abrupt drops in atmospheric pressure (1–9 Pa) and increases in wind speed (peak winds of 14–31 m/s). Evidence of dust entrainment during these formative vortex events included dust clearing from rock faces and the lander footpad, as well as formation of linear albedo features closely resembling dust devil tracks. Terrestrial field studies (Reiss, 2010) and laboratory experiments (Wells, 1984) have indicated that such reflectance variations can occur with minimal disturbance (including removal, deposition, or redistribution) of dust coating coarser (generally lower-reflectance) underlying material. On Mars, the removal of only microns of dust may be sufficient to generate observed dust devil tracks (Greeley et al., 2005, 2006; Michaels, 2006; Reiss 2014). Other evidence of erosion during formative vortex encounters included localized saltation (mostly within disturbed material around lander hardware) and surface creep of granules up to 2 mm in diameter (Charalambous et al., 2021).

Based on the traditionally cited threshold equation (Shao & Lu, 2000), only four (~25%) of the formative vortex events had peak winds speeds above the minimum threshold for entrainment of fine sand, and none were high enough to explain mobilization of dust or granules (peak winds are less than half Shao & Lu, 2000 dust and granule thresholds). It is possible that this discrepancy is partially attributed to data gaps present during turbulent events and/or increased surface roughness caused by deployed instruments, either of which could cause us to underestimate the peak wind shear felt on the surface (see Part 1 Charalambous et al., 2021, this issue). Nonetheless, it is also important to consider that the Shao and Lu (2000) expression may be inappropriate for interpreting all types of observed transport, thus adding to the discrepancy between measurements and observations. For example, the modified model provided by Merrison et al., 2007, which allows for mobilization through drag-induced rolling, has been previously utilized to explain mobilization of dust (Sullivan et al., 2008) and granules (Baker et al., 2018a; De Vet et al., 2014) on Mars. Following this model, larger particles can detach via rolling at far lower friction speeds than are required to be lifted off the bed and entrained in the wind flow (i.e., driven into saltation), effectively flattening the right side of the threshold curve as compared to the one presented in Shao and Lu (2000) (Figure 2). This modification may provide one explanation for how vortex-induced wind gusts are producing simultaneous mobilization of a wide range of grain sizes, including rolling of low-density dust aggregates observed on the InSight lander deck (Charalambous et al., 2021, this issue), redistribution of sand, and surface creep of granules.

Furthermore, as both the Shao and Lu (2000) and Merrison et al. (2007) expressions are designed for use within steady free-stream wind flows, neither considers the additional erosional forces that may be present during turbulent convective vortex encounters, such as the lift provided by the vertical pressure gradient (Hsu et al., 1976; Greeley & Iversen, 1985; Greeley et al., 2003; Neakrase & Greeley, 2010a, 2010b). Laboratory experiments and theoretical modeling have suggested that this "delta-P effect" (or "suction effect") might be particularly useful for reconciling dust lifting on Mars, with vortex thresholds for dust entrainment hypothesized to be only ~20% of canonical boundary layer thresholds (Greeley et al., 2003; Balme & Hagermann, 2006). Neakrase & Greeley (2010) demonstrated that the sediment flux in dust devils is dependent on the magnitude of the pressure drop and the exposure time at the surface (i.e., translational speed), such that small, fast-moving vortices with large pressure excursions are the most capable of lofting sediment into the atmosphere. These studies have demonstrated the potential efficacy of the pressure gradient in the entrainment of fine particles, but they also underscored the importance of in situ observations to test the validity of these models under natural conditions. As shown in Figure 2, including the effect of the delta-P force within our threshold equation (Equation 5; Greeley & Iversen, 1985 expression) preferentially impacts low-mass particles, such that the left side of the curve is reduced from Shao and Lu (2000). Although subsequent studies showed slightly modified curves from the one presented in Greeley and Iversen (1985) (e.g., Greeley et al., 2003), it is nonetheless still true that the vertical pressure gradient is highly effective at lifting dust particles and can thus facilitate removal at wind speeds that are lower than traditionally cited dust thresholds.

Here the atmospheric conditions present during convective events were found to be capable of entraining dust, saltating sand, and rolling granules – and sometimes all at once. The complex and highly dynamic nature of vortices make it challenging to model the full force balance acting on the surface during vortex encounters, especially given that APSS measurements will not always be sampling the same part of the vortex. Thus, although we cannot determine whether we sampled the most energetic part of the vortex (only a perfectly diametric encounter will probe both the maximum pressure drop within the core and the maximum tangential winds at the wall; Lorenz et al., 2016), detailed assessment of surface changes that occurred relatively close to the lander (and thus relatively close to the APSS sensor) can help us confidently correlate transport to recorded meteorological conditions. Spatially variable vortex flows are expected to generate preferential erosion in certain parts of the vortex (Michaels, 2006). The horizontal drag force caused by quickly rotating vortex winds can generate sporadic saltation and short-trajectory rolling of sand and granules respectively, in analogy to freestream boundary layer winds. In this sense, it is possible that dust lifting via sand blasting or disaggregation may be relevant at the edge of the core where tangential winds are the strongest. However, our results (in light of those of past studies) suggest that the additional lift generated by the delta-*P* effect within the vortex core provides an additional mechanism for direct lifting of low-mass dust particles. This lift force becomes less capable of overcoming normal gravitational forces as mass increases (Neakrase & Greeley, 2010), although rapid degassing has also been shown to produce localized saltation of sand grains (Bila et al., 2020). Whereas lifted dust may become suspended within the atmosphere, detachment of coarser grains (i.e., sand and granules) is expected (and observed) to be short-lived. This is consistent with the results of Michaels (2006), who found that vortices cause suspension of fine material (<10 μm) and rapid, local redistribution of coarse material (>104 μm).

The fact that ~10% of wind speeds measured since landing fell between 14 and 31 m/s (the range of peak vortex winds), but only an exceedingly small subset of these winds (namely those accompanied by significant pressure excursions) were observed to generate surface change provides further evidence for preferential erosion during vortex encounters. In other words, the unique atmospheric conditions present during a vortex encounter compared to background meteorological conditions are transiently applying higher stress on the surface and are thus facilitating sediment transport (see Part 1 for a summary of possible detachment-enhancing mechanisms). APSS measurements indicate that the background circulation at *Homestead hollow* varies seasonally, with dominant flow directions toward the southeast in winter and northwest in summer. MarsWRF predictions are relatively consistent with the observed seasonal and diurnal variations in wind direction and speed, but peak measured winds are on average 5–10 m/s higher than predicted in the model. Again, this is not necessarily surprising, given that MarsWRF is run at mesoscale resolution and thus simulated flows are more representative of the wind field averaged over a model grid cell (~4 km) and a period of minutes. In other words, mesoscale models do not resolve local-scale turbulence and will consequently underpredict the maximum shear stresses felt on the surface. This makes it difficult to predict

aeolian activity, especially given the crucial role turbulence plays in mobilizing surface material (e.g., Barchyn et al., 2014; Pähtz et al., 2018; Stout & Zobeck, 1997; Sullivan et al., 2017). Nevertheless, MarsWRF provides a sense of how regional-scale circulation patterns impact aeolian activity by controlling the direction and strength of ambient background winds, both of which will affect sensible heat flux and turbulence characteristics, control what local-scale topography influences the wind field, and may also favor or suppress vortex development (e.g., winds may provide a source of vorticity but if too strong may also disrupt vortex growth; Rafkin et al., 2016). One indication that the model does not explicitly resolve vortices (nor the increased drag they generate) can be seen in Figure 3, in which peak tangential vortex winds simulated by MarsWRF (in combination with the Rennó et al., 1998 scheme) are notably higher and display a fundamentally different seasonal trend than peak free-stream winds predicted by the model. This divergence is important to note for comparison with and interpretation of meteorological data. For example, if strong vortices passing close to InSight were to dominate APSS measurements of peak instantaneous wind speed, we might expect those measurements to align more closely with the predicted variation in tangential wind speed. However, if vortex winds do not dominate, we might expect APSS peak instantaneous winds to vary more with the predicted free-stream winds output from MarsWRF.

Thus far, the seasonality in peak APSS winds has more closely followed that predicted for free-stream winds than peak tangential winds, but it is difficult to determine the impact that the regional dust storm shortly after landing had on local atmospheric conditions. When the effects of the regional dust storm are included, by prescribing MarsWRF's dust distribution using MCS observations of the storm period (instead of using a "storm-free" dust distribution), maximum time-averaged free-stream winds are barely impacted, but tangential winds (and dust devil activity more generally) both decrease substantially. This is because the key driver of convective activity, the daytime surface-to-air temperature difference, is greatly reduced when dust opacities are high, due to more solar energy being absorbed in the atmosphere before reaching the surface. Indeed, vortex encounters were rarer and less energetic during the period when dust storm conditions were present (between L_s 330 and 30) and no surface changes were observed during this time. Continued monitoring over the duration of the mission will allow us further investigate how individually varying atmospheric conditions (including ambient wind speed, atmospheric density, and vortex activity) interact to control aeolian activity. Furthermore, future observations will help better constrain which MarsWRF outputs (e.g., free-stream wind or tangential vortex wind) are most useful for predicting vortex-induced sediment motion at this location. For example, given that the model predicts tangential winds (free-stream winds) reach a maximum (minimum) in local fall, it will be particularly interesting to observe which of these two parameters align more closely with winds sampled from APSS and with surface activity during this upcoming period of the year. Whereas the timing of surface activity observed thus far has broadly correlated with periods of increased winds and vortex activity, this activity is nonetheless highly intermittent. The stochastic nature of aeolian transport here is evidenced by the fact that two-thirds of the most energetic convective vortices recorded on the surface, including multiple with pressure drops > 5 Pa and wind gusts > 20 m/s (Spiga et al., 2020, this issue), did not produce any observable surface erosion. Even the strongest wind (~31.5 m/s, sol 364) and largest pressure excursion (~9 Pa, sol 65) sampled on the surface to date only produced minimal, localized surface changes.

As it turns out, a majority of landed spacecraft (e.g., Viking landers, Mars Pathfinder, Phoenix, and MER rovers) observed similar levels of stability at their respective field sites as is observed at *Homestead hollow* (Sagan et al., 1977; Moore et al., 1985; Sullivan et al., 2000; Geissler et al., 2010). Dust removal and local sediment redistribution (predominately within disturbed areas) at the Viking and MER landing sites were observed as a result of episodic dust storms (Geissler et al., 2010; Guinness, 1979; Moore et al., 1985). At multiple landing sites, active sediment lifting has also been observed in the form of columnar dust devils (Drake 2006; Ellehoj et al., 2010; Greeley et al., 2006; Metzger 1999). Dust devil activity was found to be particularly high within Gusev crater, where the Spirit rover imaged over seven hundred dust devils, at least one of which left a dark track in its wake (Greeley et al., 2010). The stark contrast between these observations and the paucity of dust devils imaged from InSight suggests that either (1) vortices at Gusev crater are more erosive (i.e., energetic) than those sampled at *Homestead hollow* and/or (2) local motion thresholds at Gusev are relatively lower than those at *Homestead hollow*. Unfortunately, the Spirit rover was not equipped with meteorological instruments and thus could not provide information on the strength of convective vortices at its location. At the El Dorado ripple field in Gusev, passing vortices were able to lift dust and

cause localized surface darkening without disturbing impact ripple morphologies (Sullivan et al., 2008), even though sand within ripples are theoretically easier to mobilize than dust. The authors reconciled this discrepancy by attributing mobilization of dust aggregates to a mechanism similar to that described in Merrison et al. (2007). Here we propose that the strong suction effect within the vortex core may also help explain how dust can be lifted with only minimal disturbance to surrounding sand populations. Interestingly, a subsequent dust storm was able to generate cm-scale migration of El Dorado impact ripples, underscoring the difference between the turbulent redistribution of surface material that can result from the transient passage of convective vortices and the development of organized aeolian ripples, which form in response to episodes of strong, unidirectional winds. Dust devil tracks and aeolian bedforms are both archetypal Martian surface features, but they are indicative of fundamentally different atmospheric processes.

Gale crater is geomorphically distinct from previous landing sites, in that background circulation patterns generate near-daily ripple migration during ~half of the martian year (Baker et al., 2018b). In contrast to bedforms at other landing sites, which were either immobile or only active during exceptional dust storm conditions, aeolian bedforms at Gale crater are being modified on a regular basis in response to ambient background winds. Despite widespread sand motion at this location, active dust devils have not been reported since landing (Moores et al., 2015; Streakley & Murphy 2016). Given that at least some dust is available at the surface (e.g., Arvidson et al., 2014), and unless the paucity of imaged dust devils is an observational bias (Newman et al., 2019), it would be intuitive to conclude that vortex pressure excursions need to be >3 Pa (the maximum drop recorded from MSL REMS) to lift material (Kahanpaa et al., 2016). In fact, prior to the InSight mission pressure drops above 3 Pa had rarely been recorded on the surface of Mars (Ellehoj et al., 2010; Murphy & Nelli, 2002). Despite a large number of vortices sampled at *Homestead hollow* having pressure excursions above this value, including 10 between ~5 and 9 Pa (Banerdt et al., 2020; Lorenz et al., 2021; Spiga et al., 2020), vortices at this location are apparently not generating enough erosion to substantially modify the surface or to become visibly dust-loaded themselves. Variability in environmental factors such as ambient wind speed (Rafkin et al., 2016) and boundary layer thickness (Fenton & Lorenz, 2015; Pähtz et al., 2018) can influence sediment lifting and dust devil formation. Nevertheless, aeolian surface modification is not solely dependent on atmospheric conditions but also on the properties of the substrate, including dust cover thickness (Balme 2003, Fisher 2005; Whelley & Greeley, 2006, 2008), which could help explain regional differences in dust devil activity and track formation. It is well-understood that only a relatively small subset of vortices will become dust devils, and an even smaller subset will leave a visible track in their wake, but the exact relationship between vortex activity, dust devil occurrence, and track formation is not a simple one (Cantor et al., 2006; Fisher et al., 2005; Verba et al., 2010). For example, a strong vortex passing over a thick dust layer may be able to entrain enough material to form a dust devil without significantly altering the reflectance of the surface, while an equivalent (or weaker) vortex passing over a relatively thinner layer of dust could more readily form a dust devil track even if not lifting as much material. In this light, modeling vortex-induced sediment transport requires placing these transient phenomena within the broader context of atmospheric and geologic properties of the area.

Thermal inertia and imaging data at *Homestead hollow* suggest the top layer of the surface is composed of unconsolidated fine sand mantled by a microns-thick dust coating (Golombek et al., 2020). This dust layer was mostly removed by retro-rockets during landing, creating a notably lower-albedo area of 20-meter radius around the lander (Golombek et al., 2020). New dust devil tracks observed from HiRISE since the start of the mission are often significantly fainter (or altogether invisible) within this low-albedo area (Charalambous et al., 2021, this issue), demonstrating that there may be a deficiency in susceptible surface material within the immediate vicinity of the lander. However, regionally- derived track formation rates are also relatively low (Perrin et al., 2020; Reiss & Lorenz, 2016), implying that minimal dust coverage and/or low dust removal rates may be intrinsic characteristics of this region. Dust devil track analysis suggests that Elysium Planitia is dominated by dust devils that are relatively small (<10 m wide) compared to some other locations (globally, dust devils have been observed to be up to 500 m wide; Fisher et al., 2005). Dust cover estimates are variable across landing sites (Bell et al., 2004; Fergason et al., 2012; Mellon 2000; Rogers & Bandfield et al., 2009; Ruff & Christensen, 2002), with Meridiani Planum being the lowest-albedo (and thus presumably least dusty) site, consistent with the lack of visible dust devils and dust devil tracks at this location (Golombek et al., 2005).

Dust devil tracks observed before (Reiss & Lorenz, 2016) and after (Perrin et al., 2020, this issue) InSight's landing are predominantly oriented northwest-southeast, consistent with the direction of seasonally-reversing winds predicted by atmospheric models and measured by TWINS (Banfield et al., 2020; this paper; Spiga et al., 2018). The orientation of subtle linear tracks observed from the surface (reported here and in Banerdt et al., 2020) are well-aligned with dominant flow directions at the time of vortex encounters and are also consistent with northwest-southeast winds, suggesting that these regional-scale flows also dominate at the local scale. Overall morphological similarities between dust devil tracks observed from orbit and those observed in situ suggest that they are presumably formed by equivalent atmospheric processes. However, unlike orbital tracks which were detectable in raw images, tracks observed from the surface were only discernible with image differencing, which suggests that the latter formed by a relatively smaller amount of dust removal. Given the relative strength of vortices measured from APSS, it seems likely that limited surface erosion is at least partially attributable to a deficiency in susceptible surface material, possibly due to increased cohesion. Despite the important role of sediment compaction in setting thresholds, there is no way of varying this parameter within threshold equations themselves. Close grain packing and intermixing of sand and dust can stabilize a surface against aeolian modification (see Part 1; Charalambous et al., 2021 this issue). Furthermore, the efficacy of the delta-P effect within a vortex is significantly influenced by the thickness and permeability of the surface dust layer (e.g., Bila et al., 2020). As the cohesion of a given surface results from the long-term competition between erosional and stabilizing forces, repeated and sustained periods of aeolian activity will work against gradual surface induration and will prime the surface for continued modification. This may be especially true on Mars, where the relatively lower gravity can influence, for example, the compaction of dust being continuously re-deposited on the surface through atmospheric fallout (Musiolik et al., 2018). On the other hand, long periods of inactivity will promote induration and further stabilize the bed against subsequent erosion.

It is evident that aeolian processes have contributed to the long-term surface evolution of Elysium Planitia (Grant et al., 2020, this issue; Golombek et al., 2020; Warner et al., 2020, this issue). Over 100 Myr to 1 Ga timescales, transport of fine material generated by impact bombardment has caused crater rim degradation, development of aeolian bedforms on crater rims, and significant crater infilling (Grant et al., 2020, this issue; Warner et al., 2020, this issue). After formation 400 Ma, *Homestead hollow* experienced rapid aeolian infilling that re-equilibrated the surface with the wind regime. Subsequent aeolian modification rates decreased significantly within the hollow itself, further promoting gradual induration and stability. The surrounding plains have also become significantly more deflated, lags have developed, and fine material has become trapped between rock obstacles and within nearby craters. This process has led to partial or complete infilling of many craters across the region, significantly smoothing the landscape (Grant et al., 2020, this issue; Warner et al., 2020, this issue). Surface disruption generated by new impactors might allow for intermittent episodes of bedform development, but bedforms are evidently not mobilized frequently enough in modern times to overcome gradual induration. However, relatively fresh craters on the plains, with retention ages of <100 Myr, show evidence for bedform organization and relatively recent migration (Warner et al., 2020, this issue). These bedforms are dust-covered today, but imply more favorable climate conditions for sediment transport in the recent late Amazonian epoch.

It has long been understood that changes in orbital configuration (e.g., eccentricity and obliquity) can cause climate conditions to vary over geologic timescales, which can in turn impact aeolian surface activity (Haberle et al., 2003; Newman et al., 2005). The location and morphology of aeolian bedforms observed within and adjacent to craters surrounding *Homestead hollow* are also consistent with dominant winds from the northwest and/or southeast, suggesting that contemporary flow directions may have prevailed for much of the recent geologic history of the region (Banks et al., 2019; Warner et al., 2020, this issue). However, the existence of these bedforms does indicate a divergence from current climatic conditions, as these necessarily require sustained saltation (and thus sustained free-stream winds above threshold) to form. Although a small subset of relatively smaller-scale and "fresh" (darker albedo) ripples do exist within some nearby craters (within a few kms of the landing site; Movie S4), a majority of bedforms display high albedos indicating significant dust cover and relative stability under current climatic conditions (Banks et al., 2019), consistent with the lack of bedform motion observed in HiRISE images. Although we cannot entirely rule out the possibility that bedforms are being mobilized under the modern wind regime, it would have to be occurring either (1) very rarely and/or (2) very slowly, such that no migration or changes to aeolian bedforms has been

observed in orbital images acquired at HiRISE resolution over roughly five Earth years. The juxtaposition between sparse, dust-mantled bedforms and fresh dust devil tracks suggests that ongoing aeolian modification at *Homestead hollow* is dominated by transient convective events that can locally redistribute surface material, but do not aid in bedform development or migration and result in limited net surface change over time. The intermittent vortex-induced sediment motion observed in situ from the InSight lander is consistent with this regional surface expression.

The aeolian environment at *Homestead hollow* is likely similar to morphologically similar plains regions across the planet, where infilled craters and dust-mantled TARs often co-occur with transient dust devil tracks. For example, Elysium Planitia is predicted to share a similar origin and evolution to the Gusev cratered plains (Golombek et al., 2006, 2020; Weitz et al., 2020). However, while the former may have experienced higher erosion rates in the past (Sweeney et al., 2018; Warner et al., 2020), the latter shows more evidence for sand and dust transport under modern climatic conditions. Given that aeolian modification is fundamentally controlled by how often (and under what conditions) the atmosphere is able to exert enough force on the surface to mobilize sediment, variations in the nature and frequency aeolian activity are uniquely tied to local geologic and climatic conditions. It is noteworthy that (unlike other landing sites, including Gusev; Guzewich et al., 2019; Moore et al., 1985; Sullivan et al., 2008) no surface changes were observed as a result of the dust storm that occurred early in InSight's mission, consistent with the reduction in vortex activity and peak wind speeds predicted and observed during this time. These observations suggest that *Homestead hollow* is one of the most stable landing sites and that local motion thresholds are rarely being exceeded under current climatic conditions.

5. Conclusions

In many ways, the relationship between environmental conditions on Mars and resultant aeolian surface modification remains a mystery, greatly hindering our ability to accurately predict sand transport and dust lifting. Synchronous observations of aeolian activity and high-frequency meteorological data are needed to constrain the dynamics of sediment transport and testing terrestrially-derived theories under natural martian conditions. In Part 1 (Charalambous et al., 2021, this issue) we present the record of vortex-induced surface changes observed at the InSight landing site over the first 400 sols of the mission, which correlate with abrupt pressure drops and transient wind gusts associated with convective vortex passage. When compared against current theoretical models as is done here, we are able to decipher the dominant erosive forces during convective events: a combination of the vertical pressure gradient force at the core of the vortex and the drag force generated by quickly rotating tangential winds are able to generate small-scale redistribution in surface material ranging from dust to granules. Integrative studies that utilize available ground-truth data are invaluable for addressing outstanding knowledge gaps, including with regard to the relationship between atmospheric conditions and resultant surface modification. Ultimately, achieving a predictive understanding of aeolian sediment transport on Mars is essential for interpreting the sedimentary rock record, modeling the dust cycle in climate models, and mitigating risk to landed spacecraft and future human explorers.

Acknowledgments
The authors want to acknowledge the all members of the InSight science and engineering teams who have played a role in helping plan and coordinate aeolian monitoring over the duration of the mission. In particular, the authors thank the APSS instrument team for overseeing the operation of TWINS and PS and the processing of meteorological data, as well as the Multimission Image Processing Laboratory (MIPL) at JPL for their help in processing regular ICC and IDC change detection images. The authors also acknowledge the HiRISE team for their support in acquiring multitemporal images covering the InSight landing site. The authors also want to thank our reviewers at JGR Planets for providing valuable feedback and insight. A significant portion of this work was supported by the InSight Project at the Jet Propulsion Laboratory, California Institute of Technology, under multiple contracts with the National Aeronautics and Space Administration (including Grants 80NSSC18K1621, 80NSSC18K1625, and 80NSSC18K1626). Support was also provided in part by NASA's Mars Data Analysis Program (MDAP), Grant NNX14AO96G.

Data Availability Statement

Orbital images used herein are available on the HiRISE website: https://hirise.lpl.arizona.edu/. All lander imaging and meteorological data are publicly available through the Planetary Data System (PDS) Geosciences node: https://pds-geosciences.wustl.edu/missions/insight/index.htm. MarsWRF model outputs analyzed herein can are publicly available via Figshare (Baker, 2020).

This paper is InSight Contribution Number (ICN) 162.

References

Almeida, M. P., Parteli, E. J., Andrade, J. S., & Herrmann, H. J. (2008). Giant saltation on Mars. *Proceedings of the National Academy of Sciences*, *105*(17), 6222–6226. https://doi.org/10.1073/pnas.0800202105

Antoniadi, E. M. (1930). *La planete Mars; etude basee sur les resultats obtenus avec la grande lunette de l'observatoire de Meudon et expose analytique de l'ensemble des travaux executes sur CET astre depuis 1659*. Paris: Librairie scientifique Hermann et cie.

Arvidson, R. E., Bellutta, P., Calef, F., Fraeman, A. A., Garvin, J. B., Gasnault, O. et al. (2014). Terrain physical properties derived from orbital data and the first 360 sols of Mars Science Laboratory Curiosity rover observations in Gale Crater. *Journal of Geophysical Research Planets*, *119*, 1322–1344. https://doi.org/10.1002/2013JE004605

Arvidson, R. E., Guinness, E. A., Moore, H. J., Tillman, J., & Wall, S. D. (1983). Three Mars years – Viking Lander 1 imaging observations. *Science*, *222*, 463–468. https://doi.org/10.1126/science.222.4623.463

Baas, A. C., & Sherman, D. J. (2006). Spatiotemporal variability of aeolian sand transport in a coastal dune environment. *Journal of Coastal Research*, *22*(5(225)), 1198–1205.

Bagnold, R. A. (1941). *The physics of blown sand and desert dunes*. London: Methuen.

Baker, M. M. (2020). *Output from the MarsWRF atmospheric model for the InSight landing site*. figshare. Dataset. https://doi.org/10.6084/m9.figshare.13125524.v2

Baker, M. M., Lapotre, M. G., Minitti, M. E., Newman, C. E., Sullivan, R., Weitz, C. M., et al. (2018a). The Bagnold Dunes in southern summer: Active sediment transport on Mars observed by the Curiosity rover. *Geophysical Research Letters*, *45*(17), 8853–8863. https://doi.org/10.1029/2018GL079040

Baker, M. M., Newman, C. E., Lapotre, M. G. A., Sullivan, R., Bridges, N. T., & Lewis, K. W. (2018b). Coarse sediment transport in the modern Martian environment. *Journal of Geophysical Research: Planets*, *123*, 1380–1394. https://doi.org/10.1002/2017JE005513

Balme, M., & Hagermann, A. (2006). Particle lifting at the soil-air interface by atmospheric pressure excursions in dust devils. *Geophysical Research Letters*, *33*(19), L19S01. https://doi.org/10.1029/2006GL026819

Balme, M. R., Whelley, P. L., & Greeley, R. (2003). Mars: dust devil track survey in Argyre Planitia and Hellas Basin. *Journal of Geophysical Research: Planets*, *108*(E8). https://doi.org/10.1029/2003JE002096

Banerdt, W. B., Smrekar, S. E., Banfield, D., Giardini, D., Golombek, M., Johnson, C. L., et al. (2020). Initial results from the InSight mission on Mars. *Nature Geoscience*, *13*(3), 183–189. https://doi.org/10.1038/s41561-020-0544-y

Banfield, D., Rodriguez-Manfredi, J. A., Russell, C. T., Rowe, K. M., Leneman, D., Lai, H. R., et al. (2018). InSight Auxiliary Payload Sensor Suite (APSS). *Space Science Reviews*, *215*(1), 4. https://doi.org/10.1007/s11214-018-0570-x

Banfield, D., Spiga, A., Newman, C., Forget, F., Lemmon, M., Lorenz, R., et al. (2020). The atmosphere of Mars as observed by InSight. *Nature Geoscience*, *13*(3), 190–198. https://doi.org/10.1038/s41561-020-0534-0

Banks, M. E., Baker, M. M., Warner, N. H., Newman, C. E., Lorenz, R., Golombek, M. P., & Williams, N. R. (2019). Eolian bedforms in the region surrounding the InSight landing site, Mars. *GSA Annual Meeting in Phoenix, AZ*.

Banks, M. E., Fenton, L. K., Bridges, N. T., Geissler, P. E., Chojnacki, M., Runyon, K. D., et al. (2018). Patterns in mobility and modification of middle- and high-latitude southern hemisphere dunes on Mars. *Journal of Geophysical Research: Planets*, *123*, 3205–3219. https://doi.org/10.1029/2018JE005747

Banks, M. E., Fenton, L. K., Chojnacki, M., Silvestro, S., Runyon, K. D., Zimbelman, J. R., & Geissler, P. E. (2019). Global database of aeolian bedform mobility on mars from analysis of HiRISE data. *GSA Annual Meeting in Phoenix, AZ*.

Barchyn, T. E., Martin, R. L., Kok, J. F., & Hugenholtz, C. H. (2014). Fundamental mismatches between measurements and models in aeolian sediment transport prediction: The role of small-scale variability. *Aeolian Research*, *15*, 245–251.

Bell, III, J. F., (2004). Multispectral imaging results from the Mars exploration Rover Gusev and Meridiani Landing Sites. In *AAS/Division for Planetary Sciences Meeting Abstracts# 36* (pp. 27–03).

Bila, T., Wurm, G., Onyeagusi, F. C., & Teiser, J. (2020). Lifting grains by the transient low pressure in a martian dust devil. *Icarus*, *339*, 113569. https://doi.org/10.1016/j.icarus.2019.113569

Breed, C. S., Grolier, M. J., & McCauley, J. F. (1979). Morphology and distribution of common sand dunes on Mars: Comparison with the Earth. *Journal of Geophysical Research*, *84*(B14), 8183–8204. https://doi.org/10.1029/JB084iB14p08183

Bridges, N. T., Bourke, M. C., Geissler, P. E., Banks, M. E., Colon, C., Diniega, S., et al. (2012). Planet-wide sand motion on Mars. *Geology*, *40*(1), 31–34. https://doi.org/10.1130/G32373.1

Bridges, N. T., Sullivan, R., Newman, C. E., Navarro, S., Van Beek, J., Ewing, R. C., et al. (2017). Martian aeolian activity at the Bagnold Dunes, Gale Crater: The view from the surface and orbit. *Journal of Geophysical Research: Planets*, *122*, 2077–2110. https://doi.org/10.1002/2017JE005263

Cantor, B. A., Kanak, K. M., & Edgett, K. S. (2006). Mars Orbiter Camera observations of Martian dust devils and their tracks (September 1997 to January 2006) and evaluation of theoretical vortex models. *Journal of Geophysical Research*, *111*(E12). https://doi.org/10.1029/2006JE002700

Charalambous, C., Golombek, M., Pike, T., Warner, N., Ansan, V., Hauber, E., et al. (2019). *Rock size distributions at the InSight Landing Site*. EPSC, 2019 EPSC-DPS2019.

Charalambous, C., McClean, J. B., Baker, M., Pike, W. T., Golombek, M., Lemmon, M., et al. (2021). *Aeolian changes at the InSight landing site: Multi-instrument observations*. Submitted to this issue.

Chojnacki, M., Banks, M. E., Fenton, L. K., & Urso, A. C. (2019). Boundary condition controls on the high-sand-flux regions of Mars. *Geology*, *47*, 1–4, https://doi.org/10.1130/G45793.1

Christensen, P. R., Jakosky, B. M., Kieffer, H. H., Malin, M. C., McSween, H. Y., Nealson, K., et al. (2004). The thermal emission imaging system (THEMIS) for the Mars 2001 Odyssey Mission. *Space Science Reviews*, *110*(1–2), 85–130. https://doi.org/10.1023/B:SPAC.0000021008.16305.94

Cutts, J. A., & Smith, R. S. U. (1973). Eolian deposits and dunes on Mars. *Journal of Geophysical Research*, *78*(20), 4139–4154. https://doi.org/10.1029/JB078i020p04139

Day, M., & Rebolledo, L. (2019). Intermittency in wind-driven surface alteration on Mars interpreted from wind streaks and measurements by InSight. *Geophysical Research Letters*, *46*(22), 12747–12755. https://doi.org/10.1029/2019GL085178

De Vet, S. J., Merrison, J. P., Mittelmeijer-Hazeleger, M. C., Van Loon, E. E., & Cammeraat, L. H. (2014). Effects of rolling on wind-induced detachment thresholds of volcanic glass on Mars. *Planetary and Space Science*, *103*, 205–218. https://doi.org/10.1016/j.pss.2014.07.012

Drake, N. B., Tamppari, L. K., Baker, R. D., Cantor, B. A., & Hale, A. S. (2006). Dust devil tracks and wind streaks in the North Polar Region of Mars: A study of the 2007 Phoenix Mars Lander Sites. *Geophysical Research Letters*, *33*(19), L19S02. https://doi.org/10.1029/2006GL026270

Dupont, S., Bergametti, G., Marticorena, B., & Simoëns, S. (2013). Modeling saltation intermittency. *Journal of Geophysical Research: Atmospheres*, *118*(13), 7109–7128.

Edgett, K. S., & Blumberg, D. G. (1994). Star and linear dunes on Mars. *Icarus*, *112*(2), 448–464. https://doi.org/10.1006/icar.1994.1197

Ellehoj, M. D., Gunnlaugsson, H. P., Taylor, P. A., Kahanpää, H., Bean, K. M., Cantor, B. A., et al. (2010). Convective vortices and dust devils at the Phoenix Mars mission landing site. *Journal of Geophysical Research*, *115*, E4. https://doi.org/10.1029/2009JE003413

Fenton, L. K., & Lorenz, R. (2015). Dust devil height and spacing with relation to the martian planetary boundary layer thickness. *Icarus*, *260*, 246–262. https://doi.org/10.1016/j.icarus.2015.07.028

Fenton, L. K., Toigo, A. D., & Richardson, M. I. (2005). Aeolian processes in Proctor Crater on Mars: Mesoscale modeling of dune-forming winds. *Journal of Geophysical Research*, *110*, E06005. https://doi.org/10.1029/2004JE002309

Fergason, R. L., Christensen, P. R., Golombek, M. P., & Parker, T. J. (2012). Surface properties of the Mars Science Laboratory candidate landing sites: Characterization from orbit and predictions. *Space Science Reviews*, *170*(1–4), 739–773. https://doi.org/10.1007/s11214-012-9891-3

Fisher, J. A., Richardson, M. I., Newman, C. E., Szwast, M. A., Graf, C., Basu, S., et al. (2005). A survey of Martian dust devil activity using Mars Global Surveyor Mars Orbiter Camera images. *Journal of Geophysical Research*, *110*, E3. https://doi.org/10.1029/2003JE002165

Garvin, J. B., Frawley, J. J., & Abshire, J. B. (1999). Vertical roughness of Mars from the Mars Orbiter Laser Altimeter. *Geophysical Research Letters*, *26*, 381–384.

Geissler, P. E., Sullivan, R., Golombek, M., Johnson, J. R., Herkenhoff, K., Bridges, N., et al. (2010). Gone with the wind: Eolian erasure of the Mars Rover tracks. *Journal of Geophysical Research*, *115*, E00F11. https://doi.org/10.1029/2010JE003674

Gierasch, P. J., & Goody, R. M. (1973). A model of a Martian great dust storm. *Journal of the Atmospheric Sciences*, *30*(2), 169–179. https://doi.org/10.1175/1520-0469(1973)030<0169:AMOAMG>2.0.CO;2

Golombek, M., Grott, M., Kargl, G., Andrade, J., Marshall, J., Warner, N., et al. (2018). Geology and physical properties investigations by the InSight lander. *Space Science Reviews*, *214*(5), 84. https://doi.org/10.1007/s11214-018-0512-7

Golombek, M., Huertas, A., Kipp, D., & Calef, F. (2012). Detection and characterization of rocks and rock size-frequency distributions at the final four Mars Science Laboratory landing sites. *International Journal of Manufacturing Science and Engineering*, *7*, 1–22. https://doi.org/10.1555/mars.2012.0001

Golombek, M., Kipp, D., Warner, N., Daubar, I. J., Fergason, R., Kirk, R. L., et al. (2017). Selection of the InSight landing site. *Space Science Reviews*, *211*(1–4), 5–95. https://doi.org/10.1007/s11214-016-0321-9

Golombek, M., Warner, N. H., Grant, J. A., Hauber, E., Ansan, V., Weitz, C. M., et al. (2020). Geology of the InSight landing site on Mars. *Nature Communications*, *11*(1), 1–11.

Golombek, M. P., Arvidson, R. E., Bell, J. F., Christensen, P. R., Crisp, J. A., Crumpler, L. S., et al. (2005). Assessment of Mars Exploration Rover landing site predictions. *Nature*, *436*(7047), 44–48. https://doi.org/10.1038/nature03600

Golombek, M. P., Grant, J. A., Crumpler, L. S., Greeley, R., Arvidson, R. E., & Bell, III, J. F. (2006). Erosion rates at the Mars Exploration Rover landing sites and long-term climate change on Mars. *Journal of Geophysical Research: Planets*, *111*(E12). https://doi.org/10.1029/2006JE002754

Grant, J. A., Warner, N. H., Weitz, C. M., Golombek, M. P., Wilson, S. A., Baker, M., et al. (2020). Degradation of homestead hollow at the insight landing site based on the distribution and properties of local deposits. *Journal of Geophysical Research: Planets*, *125*, e2019JE006350. https://doi.org/10.1029/2019JE006350

Greeley, R. (2002). Saltation impact as a means for raising dust on Mars. *Planetary and Space Science*, *50*(2), 151–155. https://doi.org/10.1016/S0032-0633(01)00127-1

Greeley, R., Arvidson, R., Bell Iii, J. F., Christensen, P., Foley, D., Haldemann, A., et al. (2005). Martian variable features: New insight from the Mars Express Orbiter and the Mars Exploration Rover Spirit. *Journal of Geophysical Research: Planets*, *110*, E06002. https://doi.org/10.1029/2005JE002403

Greeley, R., Balme, M. R., Iversen, J. D., Metzger, S., Mickelson, R., Phoreman, J., & White, B. (2003). Martian dust devils: Laboratory simulations of particle threshold. *Journal of Geophysical Research*, *108*, E5. https://doi.org/10.1029/2002JE001987

Greeley, R., & Iversen, J. D. (1985). *Wind as a geological process on Earth, Mars, Venus and Titan*. Cambridge, MA: Cambridge University Press, Vol. 4.

Greeley, R., Kraft, M. D., Kuzmin, R. O., & Bridges, N. T. (2000). Mars Pathfinder landing site: Evidence for a change in wind regime from lander and orbiter data. *Journal of Geophysical Research*, *105*(E1), 1829–1840. https://doi.org/10.1029/1999JE001072

Greeley, R., Leach, R., White, B., Iversen, J., & Pollack, J. (1980). Threshold windspeeds for sand on Mars - Wind tunnel simulations. *Geophysical Research Letters*, *7*, 121–124. https://doi.org/10.1029/GL007i002p00121

Greeley, R., Waller, D. A., Cabrol, N. A., Landis, G. A., Lemmon, M. T., Neakrase, L. D., et al. (2010). Gusev Crater, Mars: Observations of three dust devil seasons. *Journal of Geophysical Research*, *115*, E7. https://doi.org/10.1029/2010JE003633

Greeley, R., Whelley, P. L., Arvidson, R. E., Cabrol, N. A., Foley, D. J., Franklin, B. J., et al. (2006). Active dust devils in Gusev crater, Mars: observations from the Mars exploration rover spirit. *Journal of Geophysical Research*, *111*(E12). https://doi.org/10.1029/2006JE002743

Guinness, E. A., Arvidson, R. E., Gehret, D. C., & Bolef, L. K. (1979). Color changes at the Viking landing sites over the course of a Mars year. *Journal of Geophysical Research: Solid Earth*, *84*(B14), 8355–8364. https://doi.org/10.1029/JB084iB14p08355

Guzewich, S. D., Lemmon, M., Smith, C. L., Martínez, G., de Vicente-Retortillo, Á., Newman, C. E., et al. (2019). Mars Science Laboratory observations of the 2018/Mars year 34 global dust storm. *Geophysical Research Letters*, *46*(1), 71–79. https://doi.org/10.1029/2018GL080839

Haberle, R. M., Murphy, J. R., & Schaeffer, J. (2003). Orbital change experiments with a Mars general circulation model. *Icarus*, *161*(1), 66–89. https://doi.org/10.1016/S0019-1035(02)00017-9

Haberle, R. M., Pollack, J. B., Barnes, J. R., Zurek, R. W., Leovy, C. B., Murphy, J. R., et al. (1993). Mars atmospheric dynamics as simulated by the NASA Ames General Circulation Model: 1. The zonal-mean circulation. *Journal of Geophysical Research*, *98*(E2), 3093–3123. https://doi.org/10.1029/92JE02946

Hébrard, E., Listowski, C., Coll, P., Marticorena, B., Bergametti, G., Määttänen, A., et al. (2012). An aerodynamic roughness length map derived from extended Martian rock abundance data. *Journal of Geophysical Research*, *117*(E4).

Holstein-Rathlou, C., Gunnlaugsson, H. P., Merrison, J. P., Bean, K. M., Cantor, B. A., Davis, J. A., et al. (2010), Winds at the Phoenix landing site. *Journal of Geophysical Research*, *115*, E5. https://doi.org/10.1029/2009JE003411

Hsu, C. T., & Fattahi, B. (1976). Mechanism of tornado funnel formation. *The Physics of Fluids*, *19*(12), 1853–1857. https://doi.org/10.1063/1.861419

Kahanpää, H., Newman, C., Moores, J., Zorzano, M. P., Martín-Torres, J., Navarro, S., et al. (2016). Convective vortices and dust devils at the MSL landing site: Annual variability. *Journal of Geophysical Research: Planets*, *121*(8), 1514–1549. https://doi.org/10.1002/2016JE005027

Kok, J. F. (2010). Difference in the wind speeds required for initiation versus continuation of sand transport on Mars: Implications for dunes and dust storms. *Physical Review Letters*, *104*(7), 074502. https://doi.org/10.1103/PhysRevLett.104.074502

Kok, J. F., Parteli, E. J., Michaels, T. I., & Karam, D. B. (2012). The physics of wind-blown sand and dust. *Reports on progress in Physics*, *75*(10), 106901. https://doi.org/10.1088/0034-4885/75/10/106901

Leighton, R. B., Murray, B. C., Sharp, R. P., Allen, J. D., & Sloan, R. K. (1965). Mariner IV photography of Mars: Initial results. *Science*, *149*(3684), 627–630.
Leovy, C. E., Zurek, R. W., & Pollack, J. B. (1973). Mechanisms for Mars dust storms. *Journal of the Atmospheric Sciences*, *30*(5), 749–762. https://doi.org/10.1175/1520-0469(1973)030<0749:MFMDS>2.0.CO;2
Lorenz, R. D. (2016). Heuristic estimation of dust devil vortex parameters and trajectories from single-station meteorological observations: Application to InSight at Mars. *Icarus*, *271*, 326–337. https://doi.org/10.1016/j.icarus.2016.02.001
Lorenz, R. D., & Reiss, D. (2015). Solar panel clearing events, dust devil tracks, and in-situ vortex detections on Mars. *Icarus*, *248*, 162–164. https://doi.org/10.1016/j.icarus.2014.10.034
Lorenz, R. D., Spiga, A., Lognonné, P., Plasman, M., Newman, C. E., & Charalambous, C. (2021). The whirlwinds of Elysium: A catalog and meteorological characteristics of "dust devil" vortices observed by InSight on Mars. *Icarus*, *355*, 114119. https://doi.org/10.1016/j.icarus.2020.114119
Maki, J. N., Golombek, M., Deen, R., Abarca, H., Sorice, C., Goodsall, T., et al. (2018). The color cameras on the InSight lander. *Space Science Reviews*, *214*(6), 105. https://doi.org/10.1029/2005JE002462
McEwen, A. S., Eliason, E. M., Bergstrom, J. W., Bridges, N. T., Hansen, C. J., Delamere, W. A., et al. (2007). Mars reconnaissance orbiter's high resolution imaging science experiment (HiRISE). *Journal of Geophysical Research*, *112*, E5. https://doi.org/10.1029/2005JE002605
McLaughlin, D. B. (1954). Wind patterns and volcanoes on Mars. *The Observatory*, *74*, 166–168.
Mellon, M. T., Jakosky, B. M., Kieffer, H. H., & Christensen, P. R. (2000). High-resolution thermal inertia mapping from the Mars global surveyor thermal emission spectrometer. *Icarus*, *148*(2), 437–455. https://doi.org/10.1006/icar.2000.6503
Merrison, J. P., Gunnlaugsson, H. P., Nørnberg, P., Jensen, A. E., & Rasmussen, K. R. (2007). Determination of the wind induced detachment threshold for granular material on Mars using wind tunnel simulations. *Icarus*, *191*(2), 568–580. https://doi.org/10.1016/j.icarus.2007.04.035
Metzger, S. M., Carr, J. R., Johnson, J. R., Parker, T. J., & Lemmon, M. T. (1999). Dust devil vortices seen by the Mars Pathfinder camera. *Geophysical Research Letters*, *26*(18), 2781–2784. https://doi.org/10.1029/1999GL008341
Michaels, T. I. (2006). Numerical modeling of Mars dust devils: Albedo track generation. *Geophysical Research Letters*, *33*(19), L19S08. https://doi.org/10.1029/2006GL026268
Mischna, M. A., Lee, C., & Richardson, M. (2012). Development of a fast, accurate radiative transfer model for the Martian atmosphere, past and present. *Journal of Geophysical Research*, *117*, E10. https://doi.org/10.1029/2012JE004110
Montabone, L., Spiga, A., Kass, D. M., Kleinböhl, A., Forget, F., & Millour, E. (2020). Martian year 34 column dust climatology from Mars climate sounder observations: Reconstructed maps and model simulations. *Journal of Geophysical Research: Planets*, *125*(8), e2019JE006111. https://doi.org/10.1029/2019JE006111
Montmessin, F., Forget, F., Rannou, P., Cabane, M., & Haberle, R. M. (2004). Origin and role of water ice clouds in the Martian water cycle as inferred from a general circulation model. *Journal of Geophysical Research*, *109*, E10004. https://doi.org/10.1029/2004JE002284
Moore, H. J. (1985). The Martian dust storm of Sol 1742. *Journal of Geophysical Research*, *90*(S01), 163–174. https://doi.org/10.1029/JB090iS01p00163
Moores, J. E., Lemmon, M. T., Kahanpää, H., Rafkin, S. C., Francis, R., Pla-Garcia, J., et al. (2015). Observational evidence of a suppressed planetary boundary layer in northern Gale Crater, Mars as seen by the Navcam instrument onboard the Mars Science Laboratory rover. *Icarus*, *249*, 129–142. https://doi.org/10.1016/j.icarus.2014.09.020
Murphy, J. R., & Nelli, S. (2002). Mars Pathfinder convective vortices: Frequency of occurrence. *Geophysical Research Letters*, *29*(23), 18–21. https://doi.org/10.1029/2002GL015214
Musiolik, G., Kruss, M., Demirci, T., Schrinski, B., Teiser, J., Daerden, F., et al. (2018). Saltation under Martian gravity and its influence on the global dust distribution. *Icarus*, *306*, 25–31. https://doi.org/10.1016/j.icarus.2018.01.007
Neakrase, L. D. V., Balme, M. R., Esposito, F., Kelling, T., Klose, M., Kok, J. F., et al. (2016). Particle lifting processes in dust devils. *Space Science Reviews*, *203*(1–4), 347–376. https://doi.org/10.1007/s11214-016-0296-6
Neakrase, L. D., & Greeley, R. (2010a). Dust devil sediment flux on Earth and Mars: Laboratory simulations. *Icarus*, *206*(1), 306–318. https://doi.org/10.1016/j.icarus.2009.08.028
Neakrase, L. D., & Greeley, R. (2010b). Dust devils in the laboratory: Effect of surface roughness on vortex dynamics. *Journal of Geophysical Research*, *115*, E5. https://doi.org/10.1029/2009JE003465
Neumann, G. A., Abshire, J. B., Aharonson, O., Garvin, J. B., Sun, X., & Zuber, M. T. (2003). Mars Orbiter Laser Altimeter pulse width measurements and footprint scale roughness. *Geophysical Research Letters*, *30*(11), 1561. https://doi.org/10.1029/2003GL017048
Newman, C. E., Baker, M. M., Banfield, D. J., Banks, M., Karatekin, O., Navarro, S., et al. (2020). Using InSight wind data to validate atmospheric models and improve predictions for other locations on Mars. *AGU Fall Meeting*. Abstract # P087-08.
Newman, C. E., Gómez-Elvira, J., Marin, M., Navarro, S., Torres, J., Richardson, M. I., et al. (2017). Winds measured by the Rover Environmental Monitoring Station (REMS) during the Mars Science Laboratory (MSL) rover's Bagnold Dunes Campaign and comparison with numerical modeling using MarsWRF. *Icarus*, *291*, 203–231. https://doi.org/10.1016/j.icarus.2016.12.016
Newman, C. E., Kahanpää, H., Richardson, M. I., Martinez, G. M., Vicente-Retortillo, A., & Lemmon, M. T. (2019). MarsWRF convective vortex and dust devil predictions for Gale Crater Over 3 Mars years and comparison with MSL-REMS observations. *Journal of Geophysical Research: Planets*, *124*(12), 3442–3468. https://doi.org/10.1029/2019JE006082
Newman, C. E., Lewis, S. R., & Read, P. L. (2005). The atmospheric circulation and dust activity in different orbital epochs on Mars. *Icarus*, *174*(1), 135–160. https://doi.org/10.1016/j.icarus.2004.10.023
Newman, C. E., Lewis, S. R., Read, P. L., & Forget, F. (2002). Modeling the Martian dust cycle, 1. Representations of dust transport processes. *Journal of Geophysical Research*, *107*(5123), 6–1. https://doi.org/10.1029/2002JE001910
Newman, C. E., & Richardson, M. I. (2015). The impact of surface dust source exhaustion on the martian dust cycle, dust storms and interannual variability, as simulated by the MarsWRF General Circulation Model. *Icarus*, *257*, 47–87. https://doi.org/10.1016/j.icarus.2015.03.030
Pähtz, T., Valyrakis, M., Zhao, X. H., & Li, Z. S. (2018). The critical role of the boundary layer thickness for the initiation of aeolian sediment transport. *Geosciences*, *8*(9), 314. https://doi.org/10.3390/geosciences8090314
Perrin, C., Rodriguez, S., Jacob, A., Lucas, A., Spiga, A., Murdoch, N., et al. (2020). Monitoring of dust devil tracks around the InSight Landing Site, Mars, and comparison with in-situ atmospheric data *Geophysical Research Letters*, *47*(10), e2020GL087234. https://doi.org/10.1029/2020GL087234
Pollack, J. B., & Sagan, C. (1967). Secular changes and dark-area regeneration on Mars. *Icarus*, *6*(1–3), 434–439.
Putzig, N. E., & Mellon, M. T. (2007). Apparent thermal inertia and the surface heterogeneity of Mars. *Icarus*, *191*(1), 68–94. https://doi.org/10.1016/j.icarus.2007.05.013

Rafkin, S., Jemmett-Smith, B., Fenton, L., Lorenz, R., Takemi, T., Ito, J., & Tyler, D. (2016). Dust devil formation. *Space Science Reviews*, *203*(1–4), 183–207. https://doi.org/10.1007/s11214-016-0307-7

Reiss, D., Hoekzema, N. M., & Stenzel, O. J. (2014). Dust deflation by dust devils on Mars derived from optical depth measurements using the shadow method in HiRISE images. *Planetary and Space Science*, *93*, 54–64. https://doi.org/10.1016/j.pss.2014.01.016

Reiss, D., & Lorenz, R. D. (2016). Dust devil track survey at Elysium Planitia, Mars: implications for the InSight landing sites. *Icarus*, *266*, 315–330. https://doi.org/10.1016/j.icarus.2015.11.012

Reiss, D., Raack, J., Rossi, A. P., Di Achille, G., & Hiesinger, H. (2010). First in-situ analysis of dust devil tracks on Earth and their comparison with tracks on Mars. *Geophysical Research Letters*, *37*(14). https://doi.org/10.1029/2010GL044016

Rennó, N. O., Burkett, M. L., & Larkin, M. P. (1998). A simple thermodynamical theory for dust devils. *Journal of the Atmospheric Sciences*, *55*, 3244–3252.

Richardson, M. I., Toigo, A. D., & Newman, C. E. (2007). PlanetWRF: A general purpose, local to global numerical model for planetary atmospheric and climate dynamics. *Journal of Geophysical Research*, *112*, E9. https://doi.org/10.1029/2006JE002825

Rogers, A. D., & Bandfield, J. L. (2009). Mineralogical characterization of Mars Science Laboratory candidate landing sites from THEMIS and TES data. *Icarus*, *203*(2), 437–453. https://doi.org/10.1016/j.icarus.2009.04.020

Ruff, S. W., & Christensen, P. R. (2002). Bright and dark regions on Mars: Particle size and mineralogical characteristics based on Thermal Emission Spectrometer data. *Journal of Geophysical Research*, *107*(E12), 2–1. https://doi.org/10.1029/2001JE001580

Ryan, J. A., & Lucich, R. D. (1983). Possible dust devils, vortices on Mars. *Journal of Geophysical Research*, *88*(C15), 11005–11011. https://doi.org/10.1029/JC088iC15p11005

Sagan, C., Pieri, D., Fox, P., Arvidson, R. E., & Guinness, E. A. (1977). Particle motion on Mars inferred from the Viking lander cameras. *Journal of Geophysical Research*, *82*(28), 4430–4438. https://doi.org/10.1029/JS082i028p04430

Schofield, J. T., Barnes, J. R., Crisp, D., Haberle, R. M., Larsen, S., Magalhaes, J. A., et al. (1997). The Mars Pathfinder atmospheric structure investigation/meteorology experiment. *Science*, *278*, 1752. https://doi.org/10.1126/science.278.5344.1752

Schönfeldt, H. J. (2004). Establishing the threshold for intermittent aeolian sediment transport. *Meteorologische Zeitschrift*, 437–444. https://doi.org/10.1127/0941-2948/2004/0013-0437

Shao, Y., & Lu, H. (2000). A simple expression for wind erosion threshold friction velocity. *Journal of Geophysical Research*, *105*(D17), 22437–22443. https://doi.org/10.1029/2000JD900304

Sherman, D. J., Jackson, D. W., Namikas, S. L., & Wang, J. (1998). Wind-blown sand on beaches: an evaluation of models. *Geomorphology*, *22*(2), 113–133.

Silvestro, S., Vaz, D. A., Yizhaq, H., & Esposito, F. (2016). Dune-like dynamic of Martian Aeolian large ripples. *Geophysical Research Letters*, *43*(16), 8384–8389. https://doi.org/10.1002/2016GL070014

Smith, D. E., & Zuber, M. T. (1996). The shape of Mars and the topographic signature of the hemispheric dichotomy. *Science*, *271*, 184–188.

Spiga, A., Banfield, D., Teanby, N. A., Forget, F., Lucas, A., Kenda, B., et al. (2018). Atmospheric science with InSight. *Space Science Reviews*, *214*(7), 109. https://doi.org/10.1007/s11214-018-0543-0

Spiga, A., Murdoch, N., Lorenz, R., Forget, F., Newman, C., Rodriguez, S., et al. (2020). A study of daytime convective vortices and turbulence in the Martian planetary boundary layer based on half-a-year of InSight atmospheric measurements and large-eddy simulations. *Journal of Geophysical Research: Planets*, *126*, e2020JE006511. https://doi.org/10.1029/2020JE006511

Steakley, K., & Murphy, J. (2016). A year of convective vortex activity at Gale crater. *Icarus*, *278*, 180–193. https://doi.org/10.1016/j.icarus.2016.06.010

Stout, J., & Zobeck, T. (1997). Intermittent saltation. *Sedimentology*, *44*(5), 959–970.

Stull, R. B. (1988). *Mean boundary layer characteristics. An introduction to boundary layer meteorology* (pp. 1–27). New York, NY: Springer.

Sullivan, R., Arvidson, R., Bell, III, J. F., Gellert, R., Golombek, M., Greeley, R., & Wray, J. (2008). Wind-driven particle mobility on Mars: Insights from Mars Exploration Rover observations at "El Dorado" and surroundings at Gusev Crater. *Journal of Geophysical Research*, *113*, E06S07. https://doi.org/10.1029/2008JE003101

Sullivan, R., Greeley, R., Kraft, M., Wilson, G., Golombek, M., Herkenhoff, K., et al. (2000). Results of the Imager for Mars Pathfinder windsock experiment. *Journal of Geophysical Research*, *105*, 24547–24562. https://doi.org/10.1029/1999JE001234

Sullivan, R., & Kok, J. F. (2017). Aeolian saltation on Mars at low wind speeds. *Journal of Geophysical Research: Planets*, *122*, 2111–2143. https://doi.org/10.1002/2017JE005275

Swann, C., Sherman, D. J., & Ewing, R. C. (2020). Experimentally-derived thresholds for windblown sand on Mars. *Geophysical Research Letters*, *47*(3), e2019GL084484. https://doi.org/10.1029/2019GL084484

Sweeney, J., Warner, N. H., Ganti, V., Golombek, M. P., Lamb, M. P., Fergason, R., & Kirk, R. (2018). Degradation of 100-m-scale rocky ejecta craters at the InSight landing site on Mars and implications for surface processes and erosion rates in the Hesperian and Amazonian. *Journal of Geophysical Research: Planets*, *123*(10), 2732–2759. https://doi.org/10.1029/2018JE005618

Tanaka, K. L., Robbins, S. J., Fortezzo, C. M., Skinner Jr, J. A., & Hare, T. M. (2014). The digital global geologic map of Mars: Chronostratigraphic ages, topographic and crater morphologic characteristics, and updateed resurfacing history. *Planetary and Space Science*, *95*, 11–24. https://doi.org/10.1016/j.pss.2013.03.006

Thomas, P., & Gierasch, P. J. (1985). Dust devils on Mars. *Science*, *230*(4722), 175–177. https://doi.org/10.1126/science.230.4722.175

Toigo, A. D., Lee, C., Newman, C. E., & Richardson, M. I. (2012). The impact of resolution on the dynamics of the martian global atmosphere: Varying resolution studies with the MarsWRF GCM. *Icarus*, *221*(1), 276–288. https://doi.org/10.1016/j.icarus.2012.07.020

Tsoar, H., Greeley, R., & Peterfreund, A. R. (1979). Mars: The north polar sand sea and related wind patterns. *Journal of Geophysical Research*, *84*(B14), 8167–8180. https://doi.org/10.1029/JB084iB14p08167

Verba, C. A., Geissler, P. E., Titus, T. N., & Waller, D. (2010). Observations from the high resolution imaging science experiment (HiRISE): Martian dust devils in Gusev and Russell craters. *Journal of Geophysical Research*, *115*, E9. https://doi.org/10.1029/2009JE003498

Ward, A. W., & Doyle, K. B. (1983). Speculation on Martian north polar wind circulation and the resultant orientations of polar sand dunes. *Icarus*, *55*(3), 420–431. https://doi.org/10.1016/0019-1035(83)90112-4

Warner, N. H., Grant, J. A., Wilson, S. A., Golombek, M. P., DeMott, A., Charalambous, C., et al. (2020). An impact crater origin for the InSight landing site at Homestead Hollow, Mars: Implications for near surface stratigraphy, surface processes, and erosion rates. *Journal of Geophysical Research: Planets*, *125*(4), e2019JE006333. https://doi.org/10.1029/2019JE006333

Wells, E. N., Veverka, J., & Thomas, P. (1984). Mars: Experimental study of albedo changes caused by dust fallout. *Icarus*, *58*(3), 331–338. https://doi.org/10.1016/0019-1035(84)90079-4

Whelley, P. L., & Greeley, R. (2006). Latitudinal dependency in dust devil activity on Mars. *Journal of Geophysical Research: Planets*, *111*(E10). https://doi.org/10.1029/2006JE002677

Whelley, P. L., & Greeley, R. (2008). The distribution of dust devil activity on Mars. *Journal of Geophysical Research*, *113*, E7. https://doi.org/10.1029/2007JE002966

White, F. M. (2006). Viscous Fluid Flow (Vol. 3). New York, NY: McGraw-Hill.

Zimbelman, J. R. (2000). Non-active dunes in the Acheron Fossae region of Mars between the Viking and Mars Global Surveyor eras. *Geophysical Research Letters*, *27*(7), 1069–1072. https://doi.org/10.1029/1999GL008399

Zurek, R. W., Barnes, J. R., Haberle, R. M., Pollack, J. B., Tillman, J. E., & Leovy, C. B. (1992). In H. H. Kieffer, B. M. Jakosky, C. W. Snyder, & M. S. Matthews (Eds.) *Dynamics of the atmosphere of Mars* (pp. 835–933).